

Forearc basin stratigraphy resulting from syntectonic sedimentation during accretionary wedge growth: Insights from sandbox analogue experiments

Atsushi Noda¹, Hiroaki Koge¹, Yasuhiro Yamada², Ayumu Miyakawa³, and Juichiro Ashi⁴

¹National Institute of Advanced Industrial Science and Technology

²JAMSTEC

³Geological Survey of Japan, AIST

⁴University of Tokyo

November 22, 2022

Abstract

Forearc basin stratigraphy is expected to record a detailed history of the deformation and growth pattern of an accretionary wedge. However, the relationship between syntectonic basin sedimentation and growth of a wedge remains poorly understood, including (1) how deformation of the wedge modifies the basin stratigraphy and (2) how syntectonic sedimentation influences deformation of the wedge. In this study, we conducted scaled analogue sandbox experiments to reproduce accretionary wedges with and without syntectonic sedimentation. The results show that basin stratigraphy varied with the growth pattern of the accretionary wedge. In the case that wedge growth was dominated by trenchward accretion, the depositional area migrated landward. In contrast, prolonged underthrusting caused the sediment layers to be tilted landward and the depocenter to migrate landward. The occurrence of two types of basin stratigraphy (i.e., trenchward and landward migration of the depocenter) reflects a contrast in strength of the basal shear resistance between the inner and outer parts of the wedge due to sedimentation on the wedge. A change in the magnitude of normal stress acting on the wedge base likely influenced the mode of deformation of the wedge. A phase dominated by underthrusting can result in the combining a retro-wedge basin with a wedge-top basin, and yield a wide area of accommodation space in the forearc basin. These results suggest that forearc basin stratigraphy is influenced by the growth pattern of an accretionary wedge that is affected by syntectonic sedimentation.

1 **Forearc basin stratigraphy resulting from syntectonic**
2 **sedimentation during accretionary wedge growth:**
3 **Insights from sandbox analogue experiments**

4 **Atsushi Noda¹, Hiroaki Koge^{2*}, Yasuhiro Yamada³, Ayumu Miyakawa¹, and**
5 **Juichiro Ashi²**

6 ¹Geological Survey of Japan, National Institute of Advanced Industrial Science and Technology
7 (AIST), Central 7, Higashi 1-1-1, Tsukuba, Ibaraki 305-8567, Japan

8 ²Atmosphere and Ocean Research Institute, The University of Tokyo, 5-1-5 Kashiwanoha,
9 Kashiwa-shi, Chiba 277-8564, Japan

10 ³Japan Agency for Marine-Earth Science and Technology (JAMSTEC), 3173-25 Showa-machi,
11 Kanazawa, Yokohama 236-0001, Japan

12 **Key Points:**

- 13 • Sandbox analogue experiments were performed to examine forearc basin
14 stratigraphy deposited on a growing accretionary wedge.
- 15 • Syntectonic sedimentation stabilized the inner wedge and each successive
16 forethrust was active for long in the outer wedge.
- 17 • Changes in the stress state within and at the base of the wedge due to
18 sedimentation may modify the deformation pattern of the wedge.

*Current address, Geological Survey of Japan, National Institute of Advanced Industrial Science and
Technology, Central 7, Higashi 1-1-1, Tsukuba, Ibaraki, Japan

Corresponding author: Atsushi Noda, a.noda@aist.go.jp

Abstract

Forearc basin stratigraphy is expected to record a detailed history of the deformation and growth pattern of an accretionary wedge. However, the relationship between syntectonic basin sedimentation and growth of a wedge remains poorly understood, including (1) how deformation of the wedge modifies the basin stratigraphy and (2) how syntectonic sedimentation influences deformation of the wedge. In this study, we conducted scaled analogue sandbox experiments to reproduce accretionary wedges with and without syntectonic sedimentation. The results show that basin stratigraphy varied with the growth pattern of the accretionary wedge. In the case that wedge growth was dominated by trenchward accretion, the depositional area migrated landward. In contrast, prolonged underthrusting caused the sediment layers to be tilted landward and the depocenter to migrate landward. The occurrence of two types of basin stratigraphy (i.e., trenchward and landward migration of the depocenter) reflects a contrast in strength of the basal shear resistance between the inner and outer parts of the wedge due to sedimentation on the wedge. A change in the magnitude of normal stress acting on the wedge base likely influenced the mode of deformation of the wedge. A phase dominated by underthrusting can result in the combining a retro-wedge basin with a wedge-top basin, and yield a wide area of accommodation space in the forearc basin. These results suggest that forearc basin stratigraphy is influenced by the growth pattern of an accretionary wedge that is affected by syntectonic sedimentation.

1 Introduction

The formation of a forearc basin at an accretionary margin is controlled by deformation of the accretionary wedge, which depends on various factors including the material properties of the wedge and the décollement (friction, cohesion, and pore fluid pressure), plate convergence (obliquity and velocity), isostatic response (uplift and subsidence), and external surface processes (erosion and sedimentation) (e.g., Byrne et al., 1988; Malavieille et al., 1993; Wang & Davis, 1996; Gutscher et al., 1998; Fuller et al., 2006; Graveleau & Dominguez, 2008; Simpson, 2010; Mannu et al., 2017; Noda, 2016, 2018). Among these factors, external surface processes can strongly influence deformation of the accretionary wedge (e.g., Storti & McClay, 1995; Simpson, 2010; Cruz et al., 2011) by (1) concentrating deformation at the

51 rear of the wedge (Storti & McClay, 1995; Hardy et al., 1998), (2) reducing the
52 taper angle (Storti & McClay, 1995; Bigi et al., 2010; Simpson, 2010), (3) decreasing
53 the number of thrusts and widening the thrust spacing, which is likely caused by
54 a reduction in differential stress in the wedge due to an increase in normal stress
55 (Liu et al., 1992; Bigi et al., 2010; Simpson, 2010; Fillon, Huisman, & van der Beek,
56 2013; Zhang et al., 2019), (4) increasing the duration of folding at the upper ramp
57 tip (Storti et al., 1997), (5) prolonging the phase of underthrusting and limiting the
58 forward propagation of thrust activity (Hardy et al., 1998; Del Castello et al., 2004),
59 (6) forming a trishear zone and causing limb rotation (Wu & McClay, 2011), (7)
60 creating and reactivating out-of-sequence thrusts (Storti et al., 2000; Mannu et al.,
61 2016), (8) stabilizing the rear of the wedge and increasing the rate of migration of
62 the deformation front (Fillon, Huisman, & van der Beek, 2013), and (9) causing a
63 switch from frontal accretion to synchronous thrusting and underthrusting due to
64 local heterogeneity of the basal shear stress (Storti et al., 2000; Del Castello et al.,
65 2004; Bigi et al., 2010).

66 Forearc basin stratigraphy deposited on a deforming accretionary wedge is
67 expected to record a dynamic history of accretionary wedge growth in response to
68 the syntectonic sedimentation processes listed above. Stratigraphic records of forearc
69 basins, established from high-resolution seismic and deep-sea drilling core data, can
70 be used to understand the factors controlling sedimentation at subduction margins
71 (e.g., Moore et al., 2015). However, it can be difficult to unravel time-series evolving
72 relation between sedimentation in the basin and deformation of the wedge from only
73 field data. For this reason, forward modelling approaches, such as sandbox analogue
74 experiments, have been widely used to understand the mechanisms controlling the
75 dynamics and evolution of fold-and-thrust belts, accretionary wedges, and forearc
76 basins (e.g., Graveleau et al., 2012).

77 Few studies have performed analogue experiments with a focus on forearc
78 basin stratigraphy (Malavieille et al., 1993; Larroque et al., 1995). These studies
79 found that contraction and thickening of the retro-wedge of the accretionary body,
80 associated with backthrusts, allowed forearc basins to form. In addition, filling
81 patterns in forearc basins are influenced by the deformation style of the wedge,
82 which in turn is related to basal friction. However, these pioneering studies did not
83 control the sediment input and assumed that the forearc basin was always overfilled

84 regardless of how much accommodation space was created, with sediment supply
85 being one of the key controls on the wedge growth pattern and basin stratigraphy
86 (Noda, 2018). From a technical standpoint, the step-by-step shortening adopted by
87 these studies has the potential to change the frictional properties of active thrusts
88 from dynamic to static (c.f., Klinkmüller et al., 2016).

89 The purpose of this study is to investigate how deformation processes in an
90 accretionary wedge modify basin stratigraphy and how syntectonic sedimentation
91 influences the deformation pattern in the wedge. We performed sandbox analogue
92 experiments, focusing on controlling the sediment input with continuous shortening.
93 We examined the geometrical characteristics of the wedge, thrust activity,
94 stratigraphic patterns, and the state of stress of the wedge for cases with and
95 without syntectonic sedimentation.

96 **2 Materials and Methods**

97 **2.1 Experimental Materials**

98 In our experiments, we used a scaled two-dimensional analogue modelling
99 technique to allow results to be compared with naturally occurring geological
100 structures (e.g., Buitter, 2012; Graveleau et al., 2012). The scaled sandbox
101 experiments are based mainly on the Mohr-Coulomb behaviour of materials used for
102 the input sediment and growing wedge. Major factors controlling the shape of the
103 wedge, which is made of dry cohesionless particles, include the slope of the wedge
104 surface, the dip of the subducting plate, the internal friction of the wedge material,
105 and basal friction along the décollement (Davis et al., 1983; Dahlen, 1984). Dry
106 granular materials, such as quartz sand, display elastic–frictional plastic behaviour
107 and reproduce the non-linear deformation behaviour of brittle crustal rocks. For this
108 reason, such materials are widely used as analogue materials to simulate the brittle
109 and frictional behaviour of sedimentary rocks in an accretionary wedge (e.g., Dahlen,
110 1984; Lohrmann et al., 2003; Graveleau et al., 2012).

111 We used two types of granular material, Toyoura sand and glass microbeads.
112 Toyoura sand, a standard testing material commonly used by Japanese civil
113 engineers, is a spherical-grained quartz-rich sand with a particle size of 0.14–0.26
114 mm ($D_{50} = 0.2$ mm), a density of approximately 1600 kg m^{-3} , an internal

115 coefficient of friction $\mu = 0.59\text{--}0.68$, and a cohesion $C = 105\text{--}127$ Pa (Yamada et al.,
116 2006; Dotare et al., 2016). The glass microbeads are spherical and $0.045\text{--}0.063$ mm
117 in diameter, have a low internal coefficient of friction ($\mu_b = 0.47$) and low cohesion
118 (40 Pa), and are considered to be a suitable analogue for weaker layers (Yamada et
119 al., 2006, 2014).

120 **2.2 Model Setup**

121 The apparatus used in the experiment was a glass-sided, rectangular
122 deformation rig with internal dimensions of $100\text{ cm} \times 30\text{ cm} \times 20\text{ cm}$ deep
123 (Figure 1). A steel plate was positioned at one end with a small window below
124 it. A rigid wedge made of wood was placed next to the steel plate but was not fixed
125 to it. The wooden wedge was designed to behave like a static backstop that has a
126 higher mechanical strength than the accretionary wedge (e.g., Tsuji et al., 2015).
127 The rigidity of the backstop was used to ensure stability during the experiments and
128 for repeatability. The mobility of the backstop helped to replicate the deformable
129 nature of equivalent structures found in natural geological systems. The backstop
130 had a dip slope of 30° with a sandpaper surface. A plastic (Mylar[®]) sheet was
131 placed over the base plate of the rig and fixed to the stepper motor behind the
132 wooden wedge (left side, Figure 1). The stepper motor was used to pull the plastic
133 sheet beneath the rigid backstop at a rate of 0.5 cm/min , thereby compressing the
134 material above. The total length of horizontal shortening was about 30 cm for all of
135 the experiments.

136 Layers of sand and glass microbeads with a total thickness of 3.4 cm were
137 used in the experiments (Figure 1). The sand and glass microbeads were sprinkled
138 into the rig from a height of approximately 30 cm above the rig floor. Alternating
139 layers of blue, red, and black sand were used to help visualize the cross-sectional
140 geometry of the models without influencing the mechanical homogeneity of the
141 sand. Mechanically weak layers were created by adding a thin layer (3 mm) of
142 glass microbeads. The layers of sprinkled sand and microbeads on the basal sheet
143 represent the deep sea sediments and trench fill overlying the subducting oceanic
144 plate, respectively.

145 Experiment A1 (Exp. A1) was performed to assess how an accretionary wedge
146 grows without syntectonic sedimentation. Three other experiments (Exp. A2,
147 A3, and A4) were designed to examine how basin stratigraphy developed while
148 an accretionary wedge continuously grew (Figure 2). We sifted dry sand from at
149 least 10 cm above the surface of the accretionary wedge to fill the topographic lows
150 that had developed after each 2 cm increment of shortening. The sprinkled sand
151 was used to replicate sedimentation in a forearc/slope basin that occurs on the
152 surface of an accretionary wedge. Three different series of experiments of types
153 A2, A3, and A4 were conducted, representing constant, fluctuating, and inversely
154 fluctuating patterns of sand input, respectively. A total of 910 g of sand was added
155 to experiments A2–A4, measuring 569 cm³ in volume.

156 Time-lapse digital images were taken at 5-s intervals using a PC-based
157 controller. The images were later analyzed to calculate the geometry of the wedge
158 (Figure 3) and assess thrust activity and stratigraphic patterns in the basins for
159 Exp. A2–A4. These images were then analyzed by the digital image correlation
160 (DIC) technique to visualize the velocity field and strain rate, and thus identify
161 thrust activity within a deforming sand body (Adam et al., 2005). The method
162 calculates the displacement field of the grains with a theoretical resolution of
163 ~ 0.5 mm. The software used for the experiments was DaVis 8.0 StrainMaster
164 (LaVision, 2012).

165 **2.3 Scaling**

166 Models used in laboratory experiments should be properly scaled so that the
167 results can be considered true analogs of real geologic settings (e.g., Hubbert, 1937).
168 Experiments using granular materials such as dry quartz sand have been widely used
169 to simulate geological structures (Graveleau et al., 2012) because these materials
170 exhibit a similar behaviour to brittle rocks that respond to elastic–frictional plastic
171 deformation with pre-failure strain hardening and post-failure strain softening until
172 a dynamically constant shear load is reached (e.g., Lohrmann et al., 2003).

173 For sedimentary rocks in an accretionary wedge with mean bulk density
174 values of 2000–2500 kg m⁻³ and cohesion values of 5–20 MPa (Schumann et al.,
175 2014), the length-scale ratio of the experiment ranges from approximately $3 \times$

176 10^4 to 1×10^5 , meaning that a 1 cm model layer in an experiment corresponds
177 to 300 m to 1 km in nature. Therefore, the 3.4-cm-thick sediment layers used in
178 this experiment are equivalent to 1–3 km of strata, which is consistent with a
179 moderate trench-fill sediment thickness for a modern accretionary margin (Noda,
180 2016). The total amount of shortening from the experiments was 30–35 cm, which
181 is equivalent to 9–35 km of displacement. Assuming a plate convergence rate of
182 5 cm/year, this corresponds to $1.8\text{--}7 \times 10^5$ years. A sediment supply of 910 g
183 delivered to the topographic lows for 6×10^5 years is equivalent to a sediment
184 budget of approximately 10^6 t/year. This calculated sediment budget is similar in
185 magnitude to the sediment load of many mountain rivers in Japan and New Zealand
186 (Milliman & Syvitski, 1992), with the sedimentary influx into the Kumano Basin
187 being $50 \text{ km} \times 70 \text{ km} \times 2 \text{ km}$ over the last 4 Myr.

188 **2.4 Limitations**

189 The purpose of this study is not to replicate the evolution of a specific
190 subduction margin but instead to derive a basic geodynamic framework including
191 general features that characterize natural forearc basins. However, some caution
192 is necessary when comparing experimental observations with natural submarine
193 accretionary wedges since analogue experiments are performed with a dry,
194 homogeneous material representing the accreting sediment. Excess pore pressure
195 within the wedge and the décollement can locally produce significant changes in
196 material properties (Hubbert & Rubey, 1959) that cannot be incorporated into the
197 model. In addition, analogue sandbox experiments cannot reproduce modifications
198 in mechanical strength from high temperatures caused by diagenetic alteration
199 in a natural forearc. The experiments do not reflect the effects of the flexural
200 response and isostatic compensation of both the overriding and subducting plates,
201 which would create notable differences between our models and natural examples
202 (e.g., Schellart & Strak, 2016). The backstop is totally undeformed and fixed to
203 the side wall, so no deformation or rotation of the backstop is possible, which can
204 modify the geometry of the wedge and outflux of materials (Gutscher et al., 1996,
205 1998; Kukowski & Oncken, 2006; Albert et al., 2018). We considered syntectonic
206 sedimentation on top of the wedge in this study, but did not simulate erosional

207 forcing of the surface of the wedge (Mugnier et al., 1997; Gravelleau & Dominguez,
208 2008; Konstantinovskaya & Malavieille, 2011; Perrin et al., 2013).

209 **3 Results**

210 We conducted four experiments, with (Exp. A2–A4) and without
211 sedimentation (Exp. A1). A total of 16 experiments were performed, with 2 to
212 9 runs conducted for each case (Figure 4). Because it is commonly difficult for
213 analogue sandbox experiments to reproduce the exact same results every time, even
214 under controlled boundary conditions (cf. Santimano et al., 2015), our results also
215 showed some degree of reproducibility (Figure 4).

216 For these experiments, we analyzed the geometry of the wedge, thrust
217 activity, and basin stratigraphy. The time-series images of digital photographs,
218 DIC data, and associated movies used for the analyses can be found in the data
219 repository (Noda et al., 2019). Based on the intervals and displacement of the
220 forethrusts, the growth pattern of the wedges occurred in two stages (Figure 4).
221 Stage 1 is characterized by high-frequency, low-displacement forethrusting
222 and high-displacement backthrusting (Figures 4 and 5). Stage 2 is marked by
223 low-frequency, high-displacement forethrusting and low-displacement backthrusting.
224 These stages are comparable with those proposed by Storti et al. (2000) and Bigi
225 et al. (2010), who describe a first stage marked by a sequence of small-scale thrusts
226 that nucleated at the subduction slot, and a second stage with a growing initial
227 wedge that reaches a critical height and behaves as a backstop for further frontal
228 accretion, leading to the trenchward migration of the deformation front.

229 **3.1 Geometry**

230 Geometrical parameters of the wedge, including height (H_{w0} and H_{w1}), width
231 (L_w), and surface slope angle (α_0 , α_1 , and α_2) (Figure 3), were measured from digital
232 images for representative runs of experiments A1–A4 (Figure 6). The uplift rate
233 of the wedge height (H_{w0}) generally decreased after the transition from stage 1 to
234 2 (Figure 6a). Exp. A1 without sedimentation showed a slightly lower uplift rate
235 (0.25 cm/cm) than Exp. A2–A4 with sedimentation (0.32–0.45 cm/cm). However,

236 the rates during stage 2 are nearly the same (0.07–0.09 cm/cm) in all experiments
 237 (Exp. A1–A4).

238 The wedge width (L_w) increases with shortening in a step-like pattern,
 239 and increases abruptly when a new forethrust nucleates, but gradually decreases
 240 until another forethrust emerges (Figure 6b). This pattern closely correlates with
 241 the slope angle (α) of the wedge, which also reflects the cyclicity of forethrust
 242 development (Figure 6c). The changes in slope angle indicate a non-steady-state
 243 evolution, which contrasts with the critical taper theory of self-similar growth that
 244 suggests shape should be conserved. However, the range of slope angles is close to
 245 the critical taper angle estimated from the material properties used in this study
 246 (e.g., Dahlen, 1984). If a dry and cohesionless wedge follows the critical taper model,
 247 the critical taper angle α can be calculated from

$$\alpha = \psi_b - \psi_0 \quad (1)$$

248 with

$$\psi_0 = \frac{1}{2} \arcsin \frac{\sin \alpha}{\sin \phi} - \frac{1}{2} \alpha \quad (2)$$

$$\psi_b = \frac{1}{2} \arcsin \frac{\sin \phi_b}{\sin \phi} - \frac{1}{2} \phi_b \quad (3)$$

$$\phi = \arctan(\mu) \quad (4)$$

$$\phi_b = \arctan(\mu_b) \quad (5)$$

249 where μ is the coefficient of internal friction of the wedge with a range from 0.589 to
 250 0.675, and μ_b is the basal friction coefficient (0.47). Therefore, the critical zone
 251 of the taper angle ranges between 8.7° and 10.6° . The average slope angle α_0
 252 of Exp. A1-2 during stage 2 falls within this critical zone, and the lower limit is
 253 nearly at the minimum critical taper angle (Figure 6c). Exp. A2–A4 also show a
 254 similar cyclicity for the slope angle α_0 , but the angles are sometimes lower than the
 255 minimum critical angle ($<8.7^\circ$).

256 When the wedges are divided into inner and outer parts (Figure 3), the slope
 257 angle of the outer wedge (α_1) correlates with the cyclicity in wedge shape. The slope

258 angle (α_1) reaches a minimum when new forethrusts are initiated, as predicted by
 259 critical taper theory (Figure 6d). In contrast, the slope angle of the inner wedge
 260 (α_2) gradually decreases as shortening increases (Figure 6d). The angles α_2 for
 261 experiments with sedimentation (Exp. A2–A4) ultimately become negative.

262 **3.2 Forethrusts and backthrusts**

263 The shortening length required for the transition from stage 1 to 2 shows a
 264 positive correlation with the amount of sedimentation. The transition from stage
 265 1 to 2 for Exp. A1 ($n = 2$) occurred after 8.9 ± 0.1 cm shortening, which is the
 266 greatest shortening among the experiments of this study (Figure 7). For other
 267 experiments with sedimentation, the shortening lengths required to initiate the
 268 transition from stage 1 to 2 were 7.7 ± 0.9 cm for Exp. A2 ($n = 7$), 7.2 ± 0.9 cm for
 269 Exp. A3 ($n = 4$), and 8.2 ± 0.6 cm for Exp. A4 ($n = 3$). The smallest amount of
 270 shortening, as observed in Exp. A3, corresponds to the largest amount of sediment
 271 input during stage 1 (Figure 7). However, Exp. A4 received the smallest amount of
 272 sediment during stage 1 but showed the greatest shortening among Exp. A2–A4.

273 The shortening length required for the nucleation of a new forethrust is similar
 274 for all experiments in stage 1 (Figure 8). The shortest mean length is 1.6 ± 0.5
 275 cm for Exp. A1 and 1.7 ± 0.5 cm for Exp. A2 . Exp. A3 (2.1 ± 0.5 cm) and A4
 276 (2.0 ± 0.3 cm) yielded slightly greater lengths than those for Exp. A1 and A2, but
 277 the intervals for all of the cases overlap with the standard deviation of the mean.
 278 Distinct differences in forethrust intervals can be recognized between Exp. A1 and
 279 other experiments in stage 2. The interval for Exp. A1 (5.2 ± 0.5 cm) is about
 280 40% smaller than those for Exp. A2 (7.2 ± 1.2 cm), A3 (7.1 ± 1.6 cm), and A4
 281 (7.7 ± 1.4 cm). Shortening lengths are quite varied for each run, and no systematic
 282 difference can be found with respect to the variation in sediment input.

283 A backthrust (BT_i) is a major structural boundary between undeformed
 284 sediment layers in the retro-wedge basin and the compressively deformed inner
 285 wedge (e.g., Silver & Reed, 1988; Byrne et al., 1993). In this study, there is a
 286 large difference in the displacement rate of the backthrusts in the inner wedge
 287 (BT_i) between Exp. A1 and the other experiments (Figure 5). The rate for Exp. A1
 288 during stage 2 is 0.10 cm/cm, while those for Exp. A2–A4 are 0.03–0.04 cm/cm. In

289 stage 1, all of the experiments show a similar trend with an average displacement
290 rate of 0.22 cm/cm.

291 **3.3 Stratigraphy and Wedge Deformation**

292 In this subsection, we analyze one run from each case of Exp. A1–A4 to
293 describe the details of wedge deformation (Figures 9–12) and basin stratigraphy
294 (Figure 13).

295 ***3.3.1 Exp. A1-2: No Sediment Supply***

296 In Exp. A1-2, wedge growth was achieved by cycles of alternating wedge
297 lengthening and thickening (Figures 6), which included the following steps: (1)
298 strain was concentrated in the incoming layer at the wedge front prior to the
299 initiation of a new forethrust (Figure 9a), (2) a flat ramp fold at the wedge front
300 formed when a forethrust nucleated at a dipping angle of 25° with a conjugate
301 backthrust at a dipping angle of 40° (Figure 9b, d, and f), (3) an increase in wedge
302 length reduced the surface slope angle (Figure 9b, d, and f), (4) the root of the
303 forethrust was dragged landward by underthrusting and the hanging wall was
304 accreted to the wedge front (Figure 9c and e), (5) underthrusting thickened the
305 wedge with occasional reactivation of pre-existing forethrusts to restore the taper
306 angle (e.g., T_5 in Figure 9c), and (6) gradual narrowing of the wedge resulted in a
307 steeper surface slope.

308 The final structure of the wedge was characterized by a sequence of forethrusts
309 with uniform spacing (Figure 9). The minimum values of slope angles α_0 and α_1
310 were close to the minimum critical taper angle at 8.7° (Figure 6d). The backthrust
311 of the inner wedge (BT_i) was active throughout the experiments (Figure 5).

312 ***3.3.2 Exp. A2-4: Constant Sediment Supply***

313 In Exp. A2-4, the forethrusts of stage 2 propagated trenchward in a similar
314 manner to those in Exp. A1. A flat ramp fold popped up, and this inverted
315 triangle zone was dragged landward and accreted to the wedge front while being
316 underthrust (Figure 10). Each thrust sheet was thicker than in Exp. A1 due to
317 syntectonic sedimentation on the hanging wall and wedge front (Figure 10c and d).

318 Since sediment filled the retro-wedge basin, the backthrusts BT_i were situated more
 319 trenchward than those in Exp. A1-2 (Figure 10b). Each forethrust (T_5 , T_6 , or T_7)
 320 was accompanied by a backthrust that developed in the hanging wall during frontal
 321 accretion and underthrusting (Figure 10b-d).

322 For every 2 cm of shortening, a constant amount of sand was delivered to
 323 the topographic lows of the retro-wedge basin, the wedge-top basin, and the
 324 wedge front (Figure 2). During stage 1 (Figure 13a), most of the input sand was
 325 used to fill the retro-wedge basin. After the transition to stage 2 (10–14 cm of
 326 shortening), the sand was deposited on the wedge-top basin corresponding to the
 327 initiation of forethrust T_5 . This wedge-top basin filled up quickly and the rest of the
 328 sand overflowed to the wedge front (14 cm of shortening). New accommodation
 329 space in the trench-slope (piggy-back) basin emerged by activation of T_6 , and
 330 the depositional site prograded trenchward (18 cm of shortening). A similar
 331 overflow of the trench-slope basin was recognized at 22 cm and 26 cm of shortening.
 332 Overall, the depocenter migrated trenchward as the progressive progradation of
 333 the deformation extended trenchward. Sediment that filled the retro-wedge basin
 334 was mostly undeformed, while sedimentary layers in the trench-slope basins were
 335 compressed due to small-scale backthrusting (Figure 10).

336 ***3.3.3 Exp. A3-4: Fluctuating Sediment Supply***

337 In Exp. A3-4, a large input of sand during the early stage of the experiment
 338 (Figure 2) meant that the transition from deformation stage 1 to 2 occurred earlier
 339 than in the other experiments (Figure 7). Three forethrusts (T_4 – T_6) were generated
 340 during stage 2, and T_5 had a relatively long phase of activity (8.3 cm of shortening)
 341 compared with the average of all of the forethrusts in stage 2 (7.0 cm) (Figure 8).
 342 Underthrusting of T_5 created a roof thrust in the incoming layer that was covered
 343 with sand that had overflowed from the wedge-top basin. This underthrusting
 344 caused a reactivation and landward rotation of T_4 and uplift P_b , resulting in a
 345 combined wedge-top and retro-wedge basin (Figure 11c and d). The thrust tip of T_5
 346 propagated trenchward as a splay fault and a trishear zone formed in response to the
 347 input of sand at the wedge front, resulting in a decrease in the forethrust dip from
 348 21 to 14° (Figure 14). During the displacement on T_6 , shortening and thickening
 349 caused reactivation of T_5 and the related backthrust BT_o (Figure 11f). Finally,

350 underthrusting of the incoming layer and the thrust sheet between T_5 and T_6 raised
 351 and tilted the outer wedge landward, creating more accommodation space on the
 352 wedge top as a forearc basin (Figure 11f).

353 Sedimentation prior to 10 cm of shortening, which corresponds to the first peak
 354 in sediment supply (Figure 2), filled the retro-wedge basin and draped the thrust
 355 sheet of T_4 (Figure 13b). Displacement on T_4 led to uplift of the cover sediments,
 356 which created a topographic barrier that trapped sediments as a wedge-top basin
 357 (10–14 cm of shortening in Figure 13b). Some of the sediment supplied during the
 358 second peak (14–20 cm of shortening) bypassed the wedge-top basin and thickened
 359 the incoming layer that was in turn emplaced within the thrust sheets between T_5
 360 and T_6 (18–22 cm of shortening in Figure 13b). As continuous uplift of the outer-arc
 361 high (a break point in the surface slope of the wedge, P_b in Figure 11) created
 362 a large increase in accommodation space on the inner wedge, the final stage of
 363 sedimentation filled this combined wedge-top/retro-wedge basin (26 cm of shortening
 364 in Figures 13b).

365 **3.3.4 Exp. A4-5: Inversely Fluctuating Sediment Supply**

366 In Exp. A4-5, only two forethrusts (T_4 and T_5) were generated during stage
 367 2, which reflects the large time interval between fault formation events (Figure 8).
 368 Fault splays were formed at the thrust tip of T_4 in response to sediment input at
 369 the wedge front (Figure 12b–d). The dip angle of forethrust T_4 gradually decreased
 370 from 25° when the forethrust developed fault splays to 12.7° at 14 cm of shortening.
 371 Underthrusting of T_5 progressively rotated the thrust sheet of T_4 landward and
 372 uplifted the outer wedge P_b to the same height as P_a , generating a combined
 373 wedge-top/retro-wedge basin and yielding a slope break (Figure 12f). Finally, the
 374 wedge behaved as a single body with a forethrust (T_5) and a backthrust (BT_i).

375 Since there was a low rate of sediment input at the beginning of the
 376 experiments (2–6 cm of shortening), the retro-wedge basin was underfilled during
 377 stage 1 (Figures 13c). The large amount of sediment delivered during the first
 378 peak of sediment input filled both the wedge-top basin and the retro-wedge basin
 379 (10–14 cm of shortening). The sediment that overflowed to the wedge front (trench)
 380 thickened the incoming layer, and the fault tip developed splays during this period

381 (Figure 12b–d). Activity on forethrusts T₄ and T₅, accompanied by a long stage of
 382 underthrusting, resulted in the formation of a wide area of accommodation space on
 383 top of the wedge. However, during the second stage of maximum sediment input,
 384 the lack of accommodation space on the wedge top resulted in thickening of the
 385 trench-fill sediments (22–26 cm of shortening).

386 4 Discussion

387 4.1 Mechanical Analysis

388 Syntectonic surface processes (sedimentation and erosion) can influence the
 389 state of stress of the deforming wedge, such as the differential stress between the
 390 maximum and minimum principal stresses and the shear stress acting on the basal
 391 décollement (e.g., Simpson, 2010; Fillon, Huismans, van der Beek, & Muñoz, 2013).
 392 In this study, we calculated these stresses from the wedge surface slope (α_0 and α_1)
 393 and wedge height (H_{w_0} and H_{w_1}), based on the assumption that the wedge follows
 394 the critical taper theory (Dahlen, 1984, 1990) (Figure 15). The differential stress
 395 $\frac{1}{2}(\sigma_1 - \sigma_3)$ and basal shear stress τ_b were calculated using the following equations:

$$\frac{1}{2}(\sigma_1 - \sigma_3) = \frac{\rho g H_w \cos \alpha \sec 2\psi_0}{\csc \phi \sec 2\psi_0 - 1} \quad (6)$$

$$\tau_b = -\mu_g \sigma_n \quad (7)$$

396 with

$$\sigma_1 = \sigma_z - \frac{1}{2}(\sigma_z - \sigma_x)(1 + \sec 2\psi_0) \quad (8)$$

$$\sigma_3 = \sigma_z - \frac{1}{2}(\sigma_z - \sigma_x)(1 - \sec 2\psi_0) \quad (9)$$

$$\sigma_n = \sigma_z - \tau_{xz} \sin 2\alpha - \frac{1}{2}(\sigma_z - \sigma_x)(1 - \cos 2\alpha) \quad (10)$$

$$\sigma_z = -\rho g H_w \cos \alpha \quad (11)$$

$$\tau_{xz} = \frac{1}{2}(\sigma_z - \sigma_x) \tan 2\psi_0 \quad (12)$$

$$\frac{1}{2}(\sigma_z - \sigma_x) = \frac{-\sigma_z}{\csc \phi \cdot \sec 2\psi_0 - 1} \quad (13)$$

397 where σ_1 and σ_3 are the maximum and minimum principal stresses, respectively;
 398 ψ_0 is derived from eq. (2); μ_g is the friction coefficient of the basal décollement; σ_n

399 is the normal stress; and τ_{xz} is the shear stress along the x axis. These equations
 400 indicate that both of the differential stress and the basal shear stress are functions
 401 of α and H_w , meaning that the absolute value of the differential stress increases as
 402 the wedge height H_w increases or the slope angle α decreases. In contrast, the basal
 403 shear stress increases if H_w and/or α increase.

404 The differential stress in each experiment showed a progressive increase
 405 with shortening (Figure 16a). For example, Exp. A2-4 shows a step-wise increase
 406 in differential stress both at P_a and P_b after 8 cm of shortening (Figure 16b),
 407 which seems to correlate with sediment input. Similarly, Exp. A3-4 shows that
 408 differential stress at P_a stays constant for a certain period (21–25 cm of shortening
 409 in Figure 16c), which corresponds to the stage without significant sedimentation
 410 (Figure 6a).

411 The basal shear stress shows a similar temporal trend to the differential stress.
 412 In Exp. A1-2, which was dominated by frontal accretion throughout the experiment,
 413 the basal shear stress shows a gradual increase with shortening, but the shear stress
 414 acting at the base of the inner wedge (P_a) is always greater than that at the outer
 415 wedge (P_b) (Figure 16a). In contrast, as was demonstrated in Exp. A3 and A4 with
 416 prolonged stages of underthrusting, the basal shear stress at the outer wedge (P_b)
 417 exceeds that at the inner wedge (P_a) for the period before the second forethrust T_5
 418 had initiated (12 cm in Exp. A3 in Figure 16c and 16 cm in Exp. A4 in Figure 16d).

419 Figures 6 and 16 indicate that syntectonic sedimentation contributed to
 420 increases in wedge height (H_{w1}) and the slope angle (α_1) of the outer wedge.
 421 These responses might have led to spatial variations in the basal shear stress
 422 along the décollement and influenced the dominant mode of deformation, such
 423 as underthrusting or frontal accretion. A similar result has been reported by
 424 Del Castello et al. (2004), who suggested that variations in the basal shear
 425 resistance due to an increase in normal stress perturbed the deformation path of
 426 the wedge. Temporal variations in coupling along the plate interface may change the
 427 deformation pattern of the wedge, which could influence the basin stratigraphy.

428 The basal stress temporally drops with the nucleation cycles of new forethrusts
 429 (Figure 16). This characteristic is comparable with the drop in normal stress or

external work force when a new thrust is initiated, as predicted by numerical simulations (Del Castello & Cooke, 2007; McBeck et al., 2017, 2018).

4.2 Sedimentation and Deformation

4.2.1 *Retro-wedge Basin*

The smaller shortening length required for the transition from stage 1 to stage 2 with syntectonic sedimentation (Exp. A2–A4) could be ascribed to additional loading in the retro-wedge basin (Figure 7). The addition of the downward gravitational force and frictional force parallel to the backstop surface strengthens the shear stress at the base of the inner wedge and enhances the mechanical stability of the rear of the initial wedge (Figure 17). The rapid decrease in the displacement rate of the backthrust (BT_i) after the transition to stage 2 (Exp. A2–A4 in Figure 5) could also be related to this additional gravitational force (cf. Silver & Reed, 1988). Thus, sedimentation in the retro-wedge basin might relate to segmentation of the wedge, characterized by an outer wedge in a critical state of stress and an inner wedge in a stable state (Lohrmann et al., 2003) that acts as a dynamic backstop (cf. Kopp & Kukowski, 2003). This may generate backthrusting in the outer wedge (BT_o) instead of having BT_i accommodate a component of the landward deformation of the wedge. The landward deformation associated with BT_o for Exp. A2–A4 could account for the lower angle of the wedge-top slope α_2 (Figures 10–12). In addition, the downward force acting on the backstop increases the possibility of having the backstop subside or rotate, which would lead to a step-down of the décollement, underplating of the subducting sediments, or tectonic erosion (Strasser et al., 2009; Kimura et al., 2011; Mannu et al., 2017).

A shorter length of shortening required for the transition from stage 1 to stage 2 in the case of syntectonic sedimentation (Exp. A2–A4) could be ascribed to additional loading in the retro-wedge basin (Figure 7). Addition of the gravitational force downward and the frictional force parallel to the backstop surface strengthens the shear stress at the base of the inner wedge and enhances the mechanical stability of the rear side of the initial wedge (Figure 17). Rapid decrease of the displacement rate of the backthrust (BT_i) after the transition to stage 2 (Exp. A2–A4 in Figure 5) could also be related with this additional gravitational force (cf. Silver & Reed,

1988). This effect would be correlated to the wedge segmentation composed of outer wedge in a critical state of stress and inner wedge in a stable state (Lohrmann et al., 2003), as a dynamic backstop (cf. Kopp & Kukowski, 2003). This may stimulate development of backthrusting in the outer wedge (BT_o) instead of using the BT_i to accommodate a component of the landward deformation of the wedge. Landward deformation associated with BT_o for Exp. A2–A4 could be a reason for a lower angle of the wedge top slope α_2 (Figures 10–12). In addition, downward force acting on the backstop increases a possibility to subside or rotate the backstop, and then to lead the décollement step-down, underplating of the subducting sediments, or tectonic erosion (Strasser et al., 2009; Kimura et al., 2011; Mannu et al., 2017).

4.2.2 *Wedge-top Basin*

An increase in the normal and basal shear stress beneath the outer wedge due to underthrusting of the incoming layer plus surface sedimentation would lead to a frictional contrast between the inner and outer wedges (Figures 17 and 18). Strong coupling of the interface between the outer wedge and the décollement could dominate the underthrusting phase, with movement on the pre-existing forethrust causing uplift of the outer wedge. Once the outer-arc high (P_b) is uplifted to a point higher than the axial zone (P_a), the wedge-top basin is combined with the retro-wedge basin to generate a wide accommodation space on top of the wedge.

Previous studies have suggested that a significant amount of sediment loading could make the wedge supercritical and therefore devoid of internal deformation (Davis et al., 1983; Liu et al., 1992; Storti & McClay, 1995; Stockmal et al., 2007; Simpson, 2010; Fillon, Huisman, & van der Beek, 2013). However, our experiments showed that the sediment layers in the wedge-top basin deformed internally in response to rotation of the main forethrust and small-scale backthrusts in the hanging wall (Figures 11f and 12d). In the present study, the sediment load on the wedge-top basin was not sufficient to make the wedge supercritical.

4.2.3 *Wedge Front (Trench)*

The thickness of the incoming layer on the subducting plate shows a positive correlation with forethrust spacing (Liu et al., 1992; Marshak & Wilkerson, 1992;

491 Contardo et al., 2011). The wide spacing and reduced number of forethrusts in
492 Exp. A2–A4, in contrast to Exp. A1 (Figures 9–12 and 17), could be partly due to
493 the amount of sediment on the incoming layer at the wedge front. Underthrusting
494 of the thickened incoming layer could amplify rotation of the pre-existing thrust
495 sheet and uplift the outer-arc high (Figure 18c). This response could increase the
496 likelihood of the wedge-top basin combining with the trench-slope basin(s) to form a
497 large forearc basin.

498 Another result of the present study is that sedimentation at the wedge front
499 could temporarily seal the toe of the frontal thrust, which may result in a splay
500 fault propagating from the fault tip (Figure 14). The formation of splay faults at
501 the thrust tip owing to a gradual decrease in the thrust angle could be related to a
502 trishear-style propagation of the fault tip towards the surface (footwall triangular
503 shear zone), most likely in response to the sedimentation volume (Erslev, 1991;
504 Hardy & Allmendinger, 2011). Although the splay faults extended along the length
505 of the slip plane, stable sliding on the active fault plane may still be favorable for
506 the nucleation of a new forethrust at a trenchward site (Del Castello & Cooke,
507 2007). The mechanical weakness of uncompacted sand supplied at the wedge front
508 may be another factor that influenced the behavior of fault tips at the wedge front.

509 **4.3 Balance between Sedimentary Supply and Accommodation** 510 **Space**

511 The amount and location of sediment deposition on the deforming wedge
512 depend on the balance between the quantity of sediment delivered from the
513 hinterland and the amount of accommodation space on the wedge. The sediment
514 is typically deposited from turbidity currents and submarine landslides, which are
515 closely correlated with eustacy, climate, and tectonics, as these factors ultimately
516 control sediment production and transportation. For example, eustatic sea level
517 fluctuations, especially during regression stages, can cause large amounts of sediment
518 to be transported directly into submarine canyons (e.g., Blum & Hattier-Womack,
519 2009). On tectonic time scales, mountain building or magmatic flare-ups along
520 convergent plate boundaries can result in the production of large amounts of
521 sediment (e.g., Larsen et al., 2014; Ducea et al., 2015, 2017). In this study, we
522 attempted to simulate deposition of sediment sourced from the hinterland across

523 the strike of the subduction zone, and therefore did not consider the direct input of
524 sediment to the trench from a different source. However, trench-fill sediment at the
525 wedge front is commonly supplied from lateral (transverse) and axial (longitudinal)
526 flows in natural forearcs. The transverse sediment supply is characterized by
527 turbidity currents in submarine canyons that incise into a deforming accretionary
528 wedge with the development of submarine fans in and around the trench. The
529 Cascadia subduction zone is an example of this tectonic setting where large amounts
530 of sediment fill the trench-slope basins and overflow sediment widely covers the
531 trench, forming submarine fans (e.g., Goldfinger et al., 2017). Submarine landslides
532 at the frontal wedge slope provide another source of sediment to the wedge front
533 (Yamada et al., 2010), and are typically observed at sediment-starved, erosive
534 margins such as the Middle America Trench (von Huene et al., 2000; Harders et
535 al., 2011), the northern Hikurangi margin (Collot et al., 2001) and the Japan Trench
536 (Strasser et al., 2013). In contrast, the longitudinal sediment supply is controlled by
537 trench-parallel turbidity currents sourced from drainage areas with high sediment
538 production, as reported at Sumatra (Moore et al., 1982), eastern Makran (Bourget
539 et al., 2011), Nankai (Pickering et al., 1992), the southern Hikurangi margin (Lewis
540 et al., 1998), and the southern Lesser Antilles (Limonta et al., 2015). For the case
541 of the Nankai Trough, subduction of thickened trench-fill sediment may cause
542 out-of-sequence thrusting and uplift of the outer-arc high (Moore et al., 2015;
543 Mannu et al., 2017).

544 The accommodation space on the wedge is controlled by the pattern of wedge
545 growth, including alternating frontal accretion and underthrusting. When frontal
546 accretion is dominant (Exp. A1 and A2), a series of small trench-slope basins
547 develops trenchward (Figures 17 and 18b). In contrast, the dominance of the
548 underthrusting phase (Exp. A3 and A4) causes uplift of the outer wedge and results
549 in the formation of a large accommodation space on the wedge top (Figures 17 and
550 18c). Therefore, the forearc basin stratigraphy could be controlled by the relative
551 balance between sediment supply and the creation of accommodation space on the
552 wedge. Even if a large accommodation space is created by uplift of the outer-arc
553 high, minor sediment input to the forearc results in an underfilled basin such as
554 Lombok basin along the Sunda arc (Lüschen et al., 2011). On the other hand, a
555 large sediment supply from the hinterland, as reported for the Cascadia forearc

556 (Beeson et al., 2017), would fill the accommodation space on the wedge and result in
 557 a great thickness of trench-fill sediment, leading to a wide spacing between thrusts
 558 and between trench-slope basins.

559 **4.4 Interactions between Surface Processes and Wedge Deformation**

560 The greater shear stress at the base of the outer wedge compared with the
 561 inner wedge ($\tau_{b_0} < \tau_{b_1}$) could strengthen coupling of the interface between the wedge
 562 base and the décollement layer, leading to slip along the pre-existing forethrust
 563 surface rather than the nucleation of a new forethrust (Figure 17). The inversion
 564 of basal shear resistance could prolong underthrusting of the incoming layer and
 565 limit frontal accretion. Numerical simulations have indicated that high basal friction
 566 could extend the duration of the underthrusting phase (Burbidge & Braun, 2002;
 567 McBeck et al., 2017). Such underthrusting has been observed at Nankai (Moore
 568 et al., 2014), northern Barbados (Moore et al., 1995), and Alaska (Li et al., 2018),
 569 where undeformed trench-fill sediments on an underthrusting slab are located behind
 570 a subducting structural high. Prolonged underthrusting drags the incoming layer
 571 landward and causes the surface slope α_1 to increase. The stratigraphy in the
 572 wedge-top basin tilts landward and the depocenter migrates landward (Figure 18c).

573 When basal shear stress is lower at the outer wedge than the inner wedge
 574 ($\tau_{b_0} > \tau_{b_1}$), the initiation of a new forethrust at the wedge front means that
 575 deformation propagates trenchward (Figure 17). This scenario can lead to a low
 576 amount of uplift of the outer-arc high, a positive surface slope of α_2 , and a lack
 577 of accommodation space on top of the wedge. In this case, most of the sediment
 578 supplied from the hinterland is redirected trenchward, resulting in trenchward
 579 migration of the depocenter (Figures 17 and 18b).

580 Although underthrusting results in an increase in the slope angle at the wedge
 581 front α_1 , when the angle reaches a critical value the mode of wedge growth switches
 582 to frontal accretion in order to decrease the taper angle (Figure 17). This change
 583 results in a cessation of uplift of the outer-arc high and stabilizes the pre-existing
 584 wedge. Most of the sediment sourced from the hinterland bypasses the wedge-top
 585 basin if it is overfilled and becomes trapped in a newly developed trench-slope basin.

586 Previous studies have invoked external factors to explain the prolonged
587 underthrusting and creation of slope breaks in accretionary wedges, including the
588 subduction of high frictional materials (Mulugeta & Koyi, 1992; Lohrmann et al.,
589 2003; Miyakawa et al., 2010), variations in the cohesion of the wedge (Zhao et al.,
590 1986), subduction of a topographic high such as a seamount (Lallemand et al., 1992;
591 Morgan & Bangs, 2017), and bending of the subducting oceanic plate (Fuller et
592 al., 2006). However, the present results suggest that syntectonic sedimentation can
593 lead to a heterogeneous distribution of stress at the décollement; i.e., a higher basal
594 shear stress on the trenchward side of the wedge relative to the landward side. This
595 implies that the slope break on the wedge surface could be generated even in the
596 case of a uniform décollement without any change in subduction (e.g., velocity) of
597 the roughness or material properties of the subducting slab.

588 **5 Conclusions**

599 We performed a series of sandbox analogue experiments to examine how
600 the pattern of stratigraphy in a forearc basin responds to deformation of an
601 accretionary wedge with syntectonic sedimentation and how the pattern of
602 wedge deformation is influenced by sedimentation on the wedge surface. Basin
603 stratigraphy was found to be controlled by the dominance of frontal accretion
604 or underthrusting during the deformation phase. When frontal accretion was
605 dominant, the wedge deformation prograded trenchward along with the depocenter.
606 In contrast, when the underthrusting phase was prolonged, the incoming layer
607 of the footwall uplifted the outer wedge and an outer-arc high emerged. This
608 caused the sediment layers deposited on the wedge top to tilt landward and the
609 depocenter to migrate landward. Syntectonic sedimentation had a number of effects
610 on wedge deformation, including (1) faster stabilization of the inner wedge by filling
611 of the retro-wedge basin and (2) longer intervals between forethrust nucleation.
612 Syntectonic sedimentation on the wedge surface could cause variations in the basal
613 shear stress along the décollement, changing the style of wedge deformation (i.e.,
614 frontal accretion vs. underthrusting) and basin evolution (i.e., trenchward vs.
615 landward migration of the depocenter). The results show that basin stratigraphy
616 depends on the growth pattern of the accretionary wedge and that sedimentation
617 alone can determine the mode of deformation of the wedge.

618 **Acknowledgments**

619 This study was supported by a Grant-in-Aid for Scientific Research
620 from the Japan Society for the Promotion of Science (JSPS) (17K05687).
621 Relevant multimedia data files for this study are available on Figshare
622 (<http://doi.org/10.6084/m9.figshare.10271294>).

References

- 623 Adam, J., Urai, J., Wieneke, B., Oncken, O., Pfeiffer, K., Kukowski, N., ...
 624 Schmatz, J. (2005). Shear localisation and strain distribution during tectonic
 625 faulting—new insights from granular-flow experiments and high-resolution
 626 optical image correlation techniques. *Journal of Structural Geology*, *27*(2),
 627 283–301. doi: 10.1016/j.jsg.2004.08.008
 628
- 629 Albert, F., Kukowski, N., Tassara, A., & Oncken, O. (2018). Material transfer and
 630 subduction channel segmentation at erosive continental margins: Insights
 631 from scaled analogue experiments. *Tectonophysics*, *749*, 46–61. doi:
 632 10.1016/j.tecto.2018.10.019
- 633 Beeson, J. W., Goldfinger, C., & Fortin, W. F. (2017). Large-scale modification
 634 of submarine geomorphic features on the Cascadia accretionary wedge
 635 caused by catastrophic flooding events. *Geosphere*, *13*(5), 1713–1728. doi:
 636 10.1130/GES01388.1
- 637 Bigi, S., Di Paolo, L., Vadacca, L., & Gambardella, G. (2010). Load and unload as
 638 interference factors on cyclical behavior and kinematics of Coulomb wedges:
 639 Insights from sandbox experiments. *Journal of Structural Geology*, *32*(1),
 640 28–44. doi: 10.1016/j.jsg.2009.06.018
- 641 Blum, M. D., & Hattier-Womack, J. (2009). Climate change, sea-level change,
 642 and fluvial sediment supply to deepwater depositional systems. In B. Kneller,
 643 O. J. Martinsen, & B. McCaffrey (Eds.), *External Controls on Deep-Water*
 644 *Depositional Systems* (Vol. 92, pp. 15–39). Tulsa, Oklahoma, United States:
 645 SEPM (Society for Sedimentary Geology). doi: 10.2110/sepmsp.092.015
- 646 Bourget, J., Zaragosi, S., Ellouz-Zimmermann, N., Mouchot, N., Garlan, T.,
 647 Schneider, J.-L., ... Lallemand, S. (2011). Turbidite system architecture
 648 and sedimentary processes along topographically complex slopes: the
 649 Makran convergent margin. *Sedimentology*, *58*(2), 376–406. doi: 10.1111/
 650 j.1365-3091.2010.01168.x
- 651 Buitter, S. J. H. (2012). A review of brittle compressional wedge models.
 652 *Tectonophysics*, *530–531*, 1–17. doi: 10.1016/j.tecto.2011.12.018
- 653 Burbidge, D. R., & Braun, J. (2002). Numerical models of the evolution of
 654 accretionary wedges and fold-and-thrust belts using the distinct-element
 655 method. *Geophysical Journal International*, *148*(3), 542–561. doi:

656 10.1046/j.1365-246x.2002.01579.x

657 Byrne, D. E., Davis, D. M., & Sykes, L. R. (1988). Loci and maximum size of thrust
658 earthquakes and the mechanics of the shallow region of subduction zones.

659 *Tectonics*, 7(4), 833–857. doi: 10.1029/TC007i004p00833

660 Byrne, D. E., Wang, W.-h., & Davis, D. M. (1993). Mechanical role of backstops in
661 the growth of forearcs. *Tectonics*, 12(1), 123–144. doi: 10.1029/92TC00618

662 Collot, J.-Y., Lewis, K., Lamarche, G., & Lallemand, S. (2001). The giant Ruatoria
663 debris avalanche on the northern Hikurangi margin, New Zealand: Result

664 of oblique seamount subduction. *Journal of Geophysical Research*, 106,
665 19271–19297. doi: 10.1029/2001JB900004

666 Contardo, X. J., Kukowski, N., & Cembrano, J. M. (2011). Material transfer and
667 its influence on the formation of slope basins along the south central Chilean

668 convergent margin: Insights from scaled sandbox experiments. *Tectonophysics*,
669 513, 20–36. doi: 10.1016/j.tecto.2011.09.016

670 Cruz, L., Malinski, J., Hernandez, M., Take, A., & Hilley, G. (2011). Erosional
671 control of the kinematics of the Aconcagua fold-and-thrust belt from numerical

672 simulations and physical experiments. *Geology*, 39(5), 439–442. doi:
673 10.1130/G31675.1

674 Dahlen, F. A. (1984). Noncohesive critical coulomb wedges: An exact solution.

675 *Journal of Geophysical Research*, 89(B12), 10125–10133. doi: 10.1029/
676 JB089iB12p10125

677 Dahlen, F. A. (1990). Critical taper model of fold-and-thrust belts and accretionary
678 wedges. *Annual Review of Earth and Planetary Sciences*, 18(1), 55–99. doi: 10

679 .1146/annurev.ea.18.050190.000415

680 Davis, D., Suppe, J., & Dahlen, F. A. (1983). Mechanics of fold-and-thrust belts and
681 accretionary wedges. *Journal of Geophysical Research*, 88(B2), 1153–1172. doi:

682 10.1029/JB088iB02p01153

683 Del Castello, M., & Cooke, M. L. (2007). Underthrusting-accretion cycle: Work
684 budget as revealed by the boundary element method. *Journal of Geophysical*

685 *Research*, 112(B12404). doi: 10.1029/2007JB004997

686 Del Castello, M., Pini, G. A., & McClay, K. R. (2004). Effect of unbalanced
687 topography and overloading on Coulomb wedge kinematics: Insights from

688 sandbox modeling. *Journal of Geophysical Research*, 109(B5). doi:

- 689 10.1029/2003JB002709
- 690 Dotare, T., Yamada, Y., Adam, J., Hori, T., & Sakaguchi, H. (2016). Initiation of
691 a thrust fault revealed by analog experiments. *Tectonophysics*, *684*, 148–156.
692 doi: 10.1016/j.tecto.2015.12.023
- 693 Ducea, M. N., Bergantz, G. W., Crowley, J. L., & Otamendi, J. (2017). Ultrafast
694 magmatic buildup and diversification to produce continental crust during
695 subduction. *Geology*, *45*(3), 235–238. doi: 10.1130/G38726.1
- 696 Ducea, M. N., Paterson, S. R., & DeCelles, P. G. (2015). High-volume magmatic
697 events in subduction systems. *Elements*, *11*(2), 99–104. doi: 10.2113/
698 gselements.11.2.99
- 699 Erslev, E. A. (1991). Trishear fault-propagation folding. *Geology*, *19*(6), 617–620.
700 doi: 10.1130/0091-7613(1991)019\$;0617:TFPF\$;2.3.CO;2
- 701 Fillon, C., Huismans, R. S., & van der Beek, P. (2013). Syntectonic sedimentation
702 effects on the growth of fold-and-thrust belts. *Geology*, *41*(1), 83–86. doi: 10
703 .1130/G33531.1
- 704 Fillon, C., Huismans, R. S., van der Beek, P., & Muñoz, J. A. (2013).
705 Syntectonic sedimentation controls on the evolution of the southern Pyrenean
706 fold-and-thrust belt: Inferences from coupled tectonic-surface processes
707 models. *Journal of Geophysical Research: Solid Earth*, *118*, 5665–5680. doi:
708 10.1002/jgrb.50368
- 709 Fuller, C. W., Willett, S. D., & Brandon, M. T. (2006). Formation of forearc basins
710 and their influence on subduction zone earthquakes. *Geology*, *34*(2), 65–68.
711 doi: 10.1130/G21828.1
- 712 Goldfinger, C., Galer, S., Beeson, J., Hamilton, T., Black, B., Romsos, C., ...
713 Morey, A. (2017). The importance of site selection, sediment supply, and
714 hydrodynamics: A case study of submarine paleoseismology on the northern
715 Cascadia margin, Washington USA. *Marine Geology*, *384*, 4–46. doi:
716 10.1016/j.margeo.2016.06.008
- 717 Graveleau, F., & Dominguez, S. (2008). Analogue modelling of the interaction
718 between tectonics, erosion and sedimentation in foreland thrust belts. *Comptes
719 Rendus Geoscience*, *340*(5), 324–333. doi: 10.1016/j.crte.2008.01.005
- 720 Graveleau, F., Malavieille, J., & Dominguez, S. (2012). Experimental modelling of
721 orogenic wedges: A review. *Tectonophysics*, *538–540*, 1–66. doi: 10.1016/j

722 .tecto.2012.01.027

723 Gutscher, M.-A., Kukowski, N., Malavieille, J., & Lallemand, S. (1996). Cyclical
 724 behavior of thrust wedges: Insights from high basal friction sandbox
 725 experiments. *Geology*, *24*(2), 135–138. doi: 10.1130/0091-7613(1996)
 726 024\$;0135:CBOTWI\$;2.3.CO;2

727 Gutscher, M.-A., Kukowski, N., Malavieille, J., & Lallemand, S. (1998). Material
 728 transfer in accretionary wedges from analysis of a systematic series of
 729 analog experiments. *Journal of Structural Geology*, *20*(4), 407–416. doi:
 730 10.1016/S0191-8141(97)00096-5

731 Harders, R., Ranero, C. R., Weinrebe, W., & Behrmann, J. H. (2011). Submarine
 732 slope failures along the convergent continental margin of the Middle
 733 America Trench. *Geochemistry, Geophysics, Geosystems*, *12*(6), 1–26. doi:
 734 10.1029/2010GC003401

735 Hardy, S., & Allmendinger, R. W. (2011). Trishear: A review of kinematics,
 736 mechanics, and applications. In K. McClay, J. Shaw, & J. Suppe (Eds.),
 737 *Thrust Fault-Related Folding* (pp. 95–119). American Association of Petroleum
 738 Geologists. doi: 10.1306/1334M943429

739 Hardy, S., Duncan, C., Masek, J., & Brown, D. (1998). Minimum work, fault
 740 activity and the growth of critical wedges in fold and thrust belts. *Basin*
 741 *Research*, *10*(3), 365–373. doi: 10.1046/j.1365-2117.1998.00073.x

742 Hubbert, M. K. (1937). Theory of scale models as applied to the study of geologic
 743 structures. *Geological Society of America Bulletin*, *48*(10), 1459–1519. doi: 10
 744 .1130/GSAB-48-1459

745 Hubbert, M. K., & Rubey, W. W. (1959). role of fluid pressure in mechanics of
 746 overthrust faulting: I. Mechanics of fluid-filled porous solids and its application
 747 to overthrust faulting. *Geological Society of America Bulletin*, *70*(2), 115–166.
 748 doi: 10.1130/0016-7606(1959)70[115:ROFPIM]2.0.CO;2

749 Kimura, G., Moore, G. F., Strasser, M., Sreaton, E., Curewitz, D., Streiff, C., &
 750 Tobin, H. (2011). Spatial and temporal evolution of the megasplay fault in
 751 the Nankai Trough. *Geochemistry, Geophysics, Geosystems*, *12*(Q0A008). doi:
 752 10.1029/2010GC003335

753 Klinkmüller, M., Schreurs, G., Rosenau, M., & Kemnitz, H. (2016). Properties of
 754 granular analogue model materials: A community wide survey. *Tectonophysics*,

- 755 684, 23–38. doi: 10.1016/j.tecto.2016.01.017
- 756 Konstantinovskaya, E., & Malavieille, J. (2011). Thrust wedges with décollement
757 levels and syntectonic erosion: A view from analog models. *Tectonophysics*,
758 502(3–4), 336–350. doi: 10.1016/j.tecto.2011.01.020
- 759 Kopp, H., & Kukowski, N. (2003). Backstop geometry and accretionary mechanics of
760 the Sunda margin. *Tectonics*, 22(6, 1072). doi: 10.1029/2002TC001420
- 761 Kukowski, N., & Oncken, O. (2006). Subduction erosion: The “normal” mode
762 of fore-arc material transfer along the Chilean margin? In O. Oncken et
763 al. (Eds.), *The Andes: Active Subduction Orogeny* (pp. 217–236). Berlin,
764 Germany: Springer. doi: 10.1007/978-3-540-48684-8_10
- 765 Lallemand, S. E., Malavieille, J., & Calassou, S. (1992). Effects of oceanic ridge
766 subduction on accretionary wedges; experimental modeling and marine
767 observations. *Tectonics*, 11(6), 1301–1313. doi: 10.1029/92TC00637
- 768 Larroque, C., Calassou, S., Malavieille, J., & Chanier, F. (1995). Experimental
769 modelling of forearc basin development during accretionary wedge growth.
770 *Basin Research*, 7(3), 255–268. doi: 10.1111/j.1365-2117.1995.tb00109.x
- 771 Larsen, I. J., Montgomery, D. R., & Greenberg, H. M. (2014). The contribution
772 of mountains to global denudation. *Geology*, 42(6), 527–530. doi: 10.1130/
773 G35136.1
- 774 LaVision. (2012). Product-manual for davis 8.0 strainmaster. [Computer software
775 manual].
- 776 Lewis, K. B., Collot, J.-Y., & Lallemand, S. E. (1998). The dammed hikurangi
777 trough: A channel-fed trench blocked by subducting seamounts and their wake
778 avalanches (new zealand-france geodynz project). *Basin Research*, 10(4),
779 441–468. doi: 10.1046/j.1365-2117.1998.00080.x
- 780 Li, J., Shillington, D. J., Saffer, D. M., Bécel, A., Nedimović, M. R., Kuehn, H., ...
781 Abers, G. A. (2018). Connections between subducted sediment, pore-fluid
782 pressure, and earthquake behavior along the Alaska megathrust. *Geology*,
783 46(4), 299–302. doi: 10.1130/G39557.1
- 784 Limonta, M., Garzanti, E., Resentini, A., Andò, S., Boni, M., & Bechstädt, T.
785 (2015). Multicyclic sediment transfer along and across convergent plate
786 boundaries (Barbados, Lesser Antilles). *Basin Research*, 27(6), 696–713.
787 doi: 10.1111/bre.12095

- 788 Liu, H., McClay, K. R., & Powell, D. (1992). Physical models of thrust wedges. In
789 K. R. McClay (Ed.), *Thrust Tectonics* (pp. 71–81). London, United Kingdom:
790 Chapman & Hall.
- 791 Lohrmann, J., Kukowski, N., Adam, J., & Oncken, O. (2003). The impact of
792 analogue material properties on the geometry, kinematics, and dynamics of
793 convergent sand wedges. *Journal of Structural Geology*, *25*(10), 1691–1711.
794 doi: 10.1016/S0191-8141(03)00005-1
- 795 Lüschen, E., Müller, C., Kopp, H., Engels, M., Lutz, R., Planert, L., . . .
796 Djajadihardja, Y. S. (2011). Structure, evolution and tectonic activity of
797 the eastern Sunda forearc, Indonesia, from marine seismic investigations.
798 *Tectonophysics*, *508*, 6–21. doi: 10.1016/j.tecto.2010.06.008
- 799 Malavieille, J., Larroque, C., & Calassou, S. (1993). Modélisation expérimentale
800 des relations tectonique/sédimentation entre bassin avant-arc et prisme
801 d'accrétion. *Paris, Académie des Sciences, Comptes Rendus*, *316*(II),
802 1131–1137.
- 803 Mannu, U., Ueda, K., Willett, S. D., Gerya, T. V., & Strasser, M. (2016).
804 Impact of sedimentation on evolution of accretionary wedges: Insights from
805 high-resolution thermomechanical modeling. *Tectonics*, *35*(12), 2828–2846.
806 doi: 10.1002/2016TC004239
- 807 Mannu, U., Ueda, K., Willett, S. D., Gerya, T. V., & Strasser, M. (2017).
808 Stratigraphic signatures of forearc basin formation mechanisms. *Geochemistry,*
809 *Geophysics, Geosystems*, *18*(6), 2388–2410. doi: 10.1002/2017GC006810
- 810 Marshak, S., & Wilkerson, M. S. (1992). Effect of overburden thickness on thrust
811 belt geometry and development. *Tectonics*, *11*(3), 560–566. doi: 10.1029/
812 92TC00175
- 813 McBeck, J. A., Cooke, M. L., Herbert, J. W., Maillot, B., & Souloumiac, P. (2017).
814 Work optimization predicts accretionary faulting: An integration of physical
815 and numerical experiments. *Journal of Geophysical Research: Solid Earth*,
816 *122*(9), 7485–7505. doi: 10.1002/2017JB013931
- 817 McBeck, J. A., Cooke, M. L., Souloumiac, P., Maillot, B., & Mary, B. (2018).
818 The influence of detachment strength on the evolving deformational energy
819 budget of physical accretionary prisms. *Solid Earth*, *9*(6), 1421–1436. doi:
820 10.5194/se-9-1421-2018

- 821 Milliman, J. D., & Syvitski, J. P. M. (1992). Geomorphic/tectonic control of
822 sediment discharge to the ocean: The importance of small mountainous rivers.
823 *Journal of Geology*, *100*(5), 525–544. doi: 10.1086/629606
- 824 Miyakawa, A., Yamada, Y., & Matsuoka, T. (2010). Effect of increased shear stress
825 along a plate boundary fault on the formation of an out-of-sequence thrust
826 and a break in surface slope within an accretionary wedge, based on numerical
827 simulations. *Tectonophysics*, *484*, 127–138. doi: 10.1016/j.tecto.2009.08.037
- 828 Moore, G. F., Boston, B. B., Strasser, M., Underwood, M. B., & Ratliff, R. A.
829 (2015). Evolution of tectono-sedimentary systems in the Kumano Basin,
830 Nankai Trough forearc. *Marine and Petroleum Geology*, *67*, 604–616. doi:
831 10.1016/j.marpetgeo.2015.05.032
- 832 Moore, G. F., Curray, J. R., & Emmel, F. J. (1982). Sedimentation in the Sunda
833 Trench and forearc region. In J. K. Leggett (Ed.), *Trench-Forearc Geology:
834 Sedimentation and Tectonics on Modern and Ancient Active Plate Margins*
835 (Vol. 10, pp. 245–258). London, United Kingdom: Geological Society.
- 836 Moore, G. F., Kanagawa, K., Strasser, M., Dugan, B., Maeda, L., Toczko, S., &
837 the IODP Expedition 338 Scientific Party. (2014). IODP Expedition 338:
838 NanTroSEIZE Stage 3: NanTroSEIZE plate boundary deep riser 2. *Scientific
839 Drilling*, *17*, 1–12. doi: 10.5194/sd-17-1-2014
- 840 Moore, G. F., Zhao, Z., Shipley, T. H., Bangs, N., & Moore, J. C. (1995). Structural
841 setting of the Leg 156 area, northern Barbados Ridge accretionary prism. In
842 T. H. Shipley, Y. Ogawa, P. Blum, & et al. (Eds.), *Proceedings of the Ocean
843 Drilling Program, Initial Reports* (Vol. 156, pp. 13–27). College Station, TX:
844 Ocean Drilling Program. doi: 10.2973/odp.proc.ir.156.102.1995
- 845 Morgan, J. K., & Bangs, N. L. (2017). Recognizing seamount-forearc collisions at
846 accretionary margins: Insights from discrete numerical simulations. *Geology*,
847 *45*(7), 635–638. doi: 10.1130/G38923.1
- 848 Mugnier, J. L., Baby, P., Colletta, B., Vinour, P., Bale, P., & Leturmy, P. (1997).
849 Thrust geometry controlled by erosion and sedimentation: A view from
850 analogue models. *Geology*, *25*(5), 427–430. doi: 10.1130/0091-7613(1997)
851 025\$;0427:TGCBEA\$;2.3.CO;2
- 852 Mulugeta, G., & Koyi, H. (1992). Episodic accretion and strain partitioning in
853 a model sand wedge. *Tectonophysics*, *202*(2), 319–333. doi: 10.1016/0040

- 854 -1951(92)90117-O
- 855 Noda, A. (2016). Forearc basins: Types, geometries, and relationships to subduction
856 zone dynamics. *Geological Society of America Bulletin*, *128*(5–6), 879–895. doi:
857 10.1130/B31345.1
- 858 Noda, A. (2018). Forearc basin stratigraphy and interactions with accretionary
859 wedge growth according to the critical taper concept. *Tectonics*, *37*(3),
860 965–988. doi: 10.1002/2017TC004744
- 861 Noda, A., Koge, H., Yamada, Y., Miyakawa, A., & Ashi, J. (2019). *Supporting*
862 *information for “Subduction of trench-fill sediments beneath an accretionary*
863 *wedges: Insights from sandbox analogue experiments”*. doi: 10.6084/
864 m9.figshare.10263674
- 865 Perrin, C., Clemenzi, L., Malavieille, J., Molli, G., Taboada, A., & Dominguez,
866 S. (2013). Impact of erosion and décollements on large-scale faulting and
867 folding in orogenic wedges: analogue models and case studies. *Journal of the*
868 *Geological Society, London*, *170*(6), 893–904. doi: 10.1144/jgs2013-012
- 869 Pickering, K. T., Underwood, M. B., & Taira, A. (1992). Open-ocean to trench
870 turbidity-current flow in the Nankai Trough: Flow collapse and reflection.
871 *Geology*, *20*(12), 1099–1102. doi: 10.1130/0091-7613(1992)020\$;1099:
872 OOTTTTC\$;2.3.CO;2
- 873 Santimano, T., Rosenau, M., & Oncken, O. (2015). Intrinsic versus extrinsic
874 variability of analogue sand-box experiments –Insights from statistical analysis
875 of repeated accretionary sand wedge experiments. *Journal of Structural*
876 *Geology*, *75*, 80–100. doi: 10.1016/j.jsg.2015.03.008
- 877 Schellart, W. P., & Strak, V. (2016). A review of analogue modelling of geodynamic
878 processes: Approaches, scaling, materials and quantification, with an
879 application to subduction experiments. *Journal of Geodynamics*, *100*, 7–32.
880 doi: 10.1016/j.jog.2016.03.009
- 881 Schumann, K., Behrmann, J. H., Stipp, M., Yamamoto, Y., Kitamura, Y., & Lempp,
882 C. (2014). Geotechnical behavior of mudstones from the Shimanto and Boso
883 accretionary complexes, and implications for the Nankai accretionary prism.
884 *Earth, Planets and Space*, *66*(1), 129. doi: 10.1186/1880-5981-66-129
- 885 Silver, E. A., & Reed, D. L. (1988). Backthrusting in accretionary wedges. *Journal*
886 *of Geophysical Research*, *93*(B4), 3116–3126. doi: 10.1029/JB093iB04p03116

- 887 Simpson, G. D. H. (2010). Formation of accretionary prisms influenced by sediment
888 subduction and supplied by sediments from adjacent continents. *Geology*,
889 *38*(2), 131–134. doi: 10.1130/G30461.1
- 890 Stockmal, G. S., Beaumont, C., Nguyen, M., & Lee, B. (2007). Mechanics
891 of thin-skinned fold-and-thrust belts: Insights from numerical models.
892 In J. W. Sears, T. A. Harms, & C. A. Evenchick (Eds.), *Whence the*
893 *Mountains? Inquiries into the Evolution of Orogenic Systems* (Vol. 433,
894 pp. 63–98). Boulder, Colorado, USA: Geological Society of America. doi:
895 10.1130/2007.2433(04)
- 896 Storti, F., & McClay, K. (1995). Influence of syntectonic sedimentation on thrust
897 wedges in analogue models. *Geology*, *23*(11), 999–1002. doi: 10.1130/0091
898 -7613(1995)023<0999:IOSSOT>2.3.CO;2
- 899 Storti, F., Salvini, F., & McClay, K. (1997). Fault-related folding in sandbox
900 analogue models of thrust wedges. *Journal of Structural Geology*, *19*(3),
901 583–602. doi: 10.1016/S0191-8141(97)83029-5
- 902 Storti, F., Salvini, F., & McClay, K. (2000). Synchronous and velocity-partitioned
903 thrusting and thrust polarity reversal in experimentally produced,
904 doubly-vergent thrust wedges: Implications for natural orogens. *Tectonics*,
905 *19*, 378–396. doi: 10.1029/1998TC001079
- 906 Strasser, M., Kölling, M., Ferreira, C. d. S., Fink, H. G., Fujiwara, T., Henkel,
907 S., ... scientists, J. C. M.-E. (2013). A slump in the trench: Tracking the
908 impact of the 2011 Tohoku-Oki earthquake. *Geology*, *41*(8), 935–938. doi:
909 10.1130/G34477.1
- 910 Strasser, M., Moore, G. F., Kimura, G., Kitamura, Y., Kopf, A. J., Lallemand,
911 S., ... Zhao, X. (2009). Origin and evolution of a splay fault in the
912 Nankai accretionary wedge. *Nature Geoscience*, *2*(9), 648–652. doi:
913 10.1038/NGEO609
- 914 Tsuji, T., Ashi, J., Strasser, M., & Kimura, G. (2015). Identification of the static
915 backstop and its influence on the evolution of the accretionary prism in the
916 Nankai Trough. *Earth and Planetary Science Letters*, *431*, 15–25. doi:
917 10.1016/j.epsl.2015.09.011
- 918 von Huene, R., Ranero, C. R., Weinrebe, W., & Hinz, K. (2000). Quaternary
919 convergent margin tectonics of Costa Rica, segmentation of the Cocos

- 920 Plate, and Central American volcanism. *Tectonics*, *19*(2), 314–334. doi:
921 10.1029/1999TC001143
- 922 Wang, W.-H., & Davis, D. M. (1996). Sandbox model simulation of forearc
923 evolution and noncritical wedges. *Journal of Geophysical Research*, *101*(B5),
924 11329–11339. doi: 10.1029/96JB00101
- 925 Wu, J., & McClay, K. (2011). Two-dimensional analog modeling of fold and
926 thrust belts: Dynamic interactions with syncontractional sedimentation and
927 erosion. In K. McClay, J. Shaw, & J. Suppe (Eds.), *Thrust Fault-Related*
928 *Folding* (pp. 301–333). American Association of Petroleum Geologists. doi:
929 10.1306/13251343M9450
- 930 Yamada, Y., Baba, K., Miyakawa, A., & Matsuoka, T. (2014). Granular experiments
931 of thrust wedges: Insights relevant to methane hydrate exploration at the
932 Nankai accretionary prism. *Marine and Petroleum Geology*, *51*, 34–48. doi:
933 10.1016/j.marpetgeo.2013.11.008
- 934 Yamada, Y., Kaneda, K., & Matsuoka, T. (2006). Influences of material properties
935 on analogue model experiments of geologic structures. *Journal of the Society of*
936 *Materials Science, Japan*, *55*(5), 452–457. (in Japanese with English abstract)
937 doi: 10.2472/jsms.55.452
- 938 Yamada, Y., Yamashita, Y., & Yamamoto, Y. (2010). Submarine landslides at
939 subduction margins: Insights from physical models. *Tectonophysics*, *484*(1),
940 156–167. doi: 10.1016/j.tecto.2009.09.007
- 941 Zhang, Y., Yang, S., Chen, H., Dilek, Y., Cheng, X., Lin, X., . . . Zhu, T. (2019).
942 The effect of overburden thickness on deformation mechanisms in the
943 Keping fold-thrust belt, southwestern Chinese Tian Shan Mountains:
944 Insights from analogue modeling. *Tectonophysics*, *753*, 79–92. doi:
945 10.1016/j.tecto.2019.01.005
- 946 Zhao, W. L., Davis, D. M., Dahlen, F. A., & Suppe, J. (1986). Origin of convex
947 accretionary wedges: Evidence from barbados. *Journal of Geophysical*
948 *Research*, *91*(B10), 10246–10258. doi: 10.1029/JB091iB10p10246

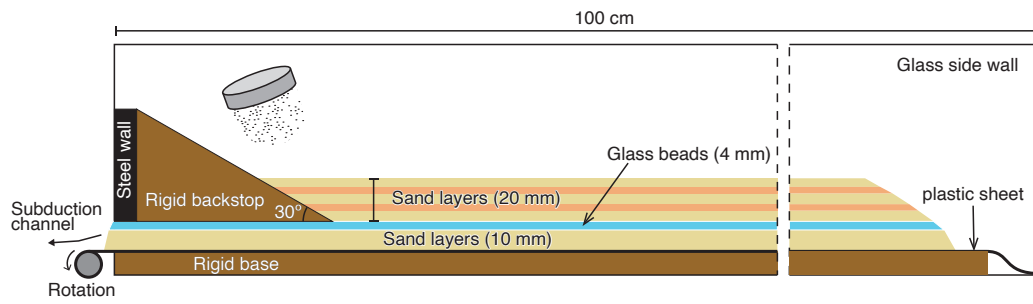


Figure 1. Experimental apparatus of this study.

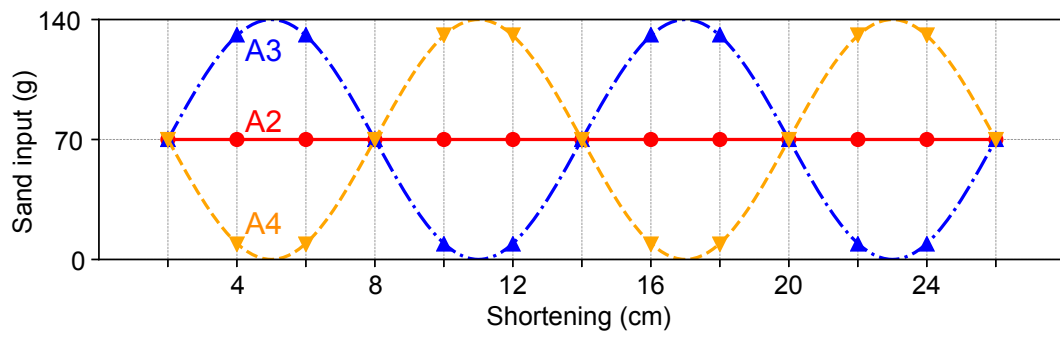


Figure 2. Amounts of sediment input during the experiments. Exp. A2, constant; Exp. A3, fluctuating; Exp. A4, inversely fluctuating.

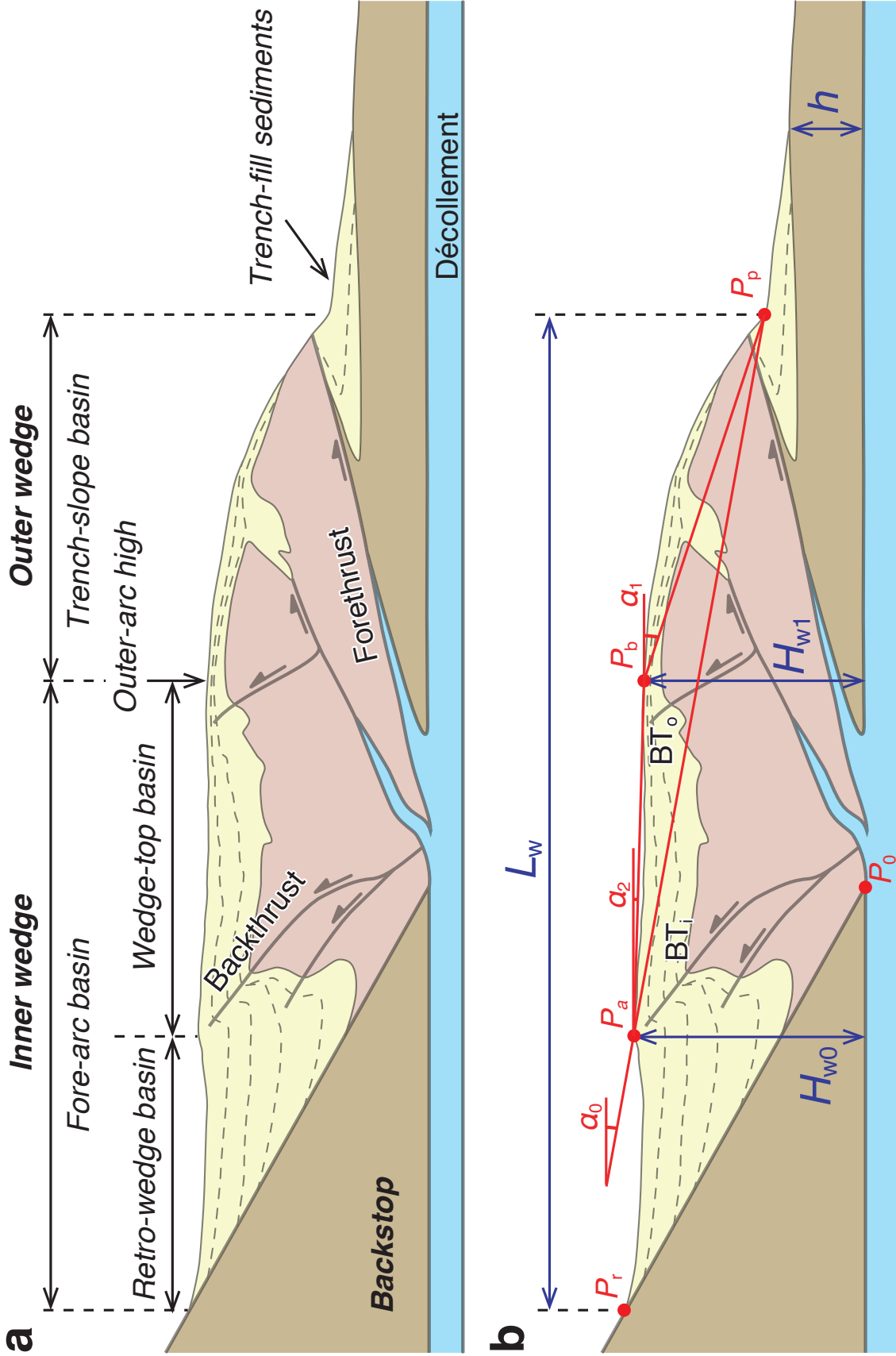


Figure 3. (a) Definition of the terminology used in this study. (b) Geometrical parameters and symbols for reference. L_w , width of the wedge; H_w , height of the wedge; h , thickness of the incoming layer (trench-fill sediment deposited on the subducting plate); P_a , axial point in the inner wedge; P_b , outer-arc high. BT_i and BT_o are backthrusts in the inner wedge and outer wedge, respectively. Slope angles of α_0 , α_2 are the angles between P_r - P_a , P_p - P_b , and P_a - P_b , respectively.

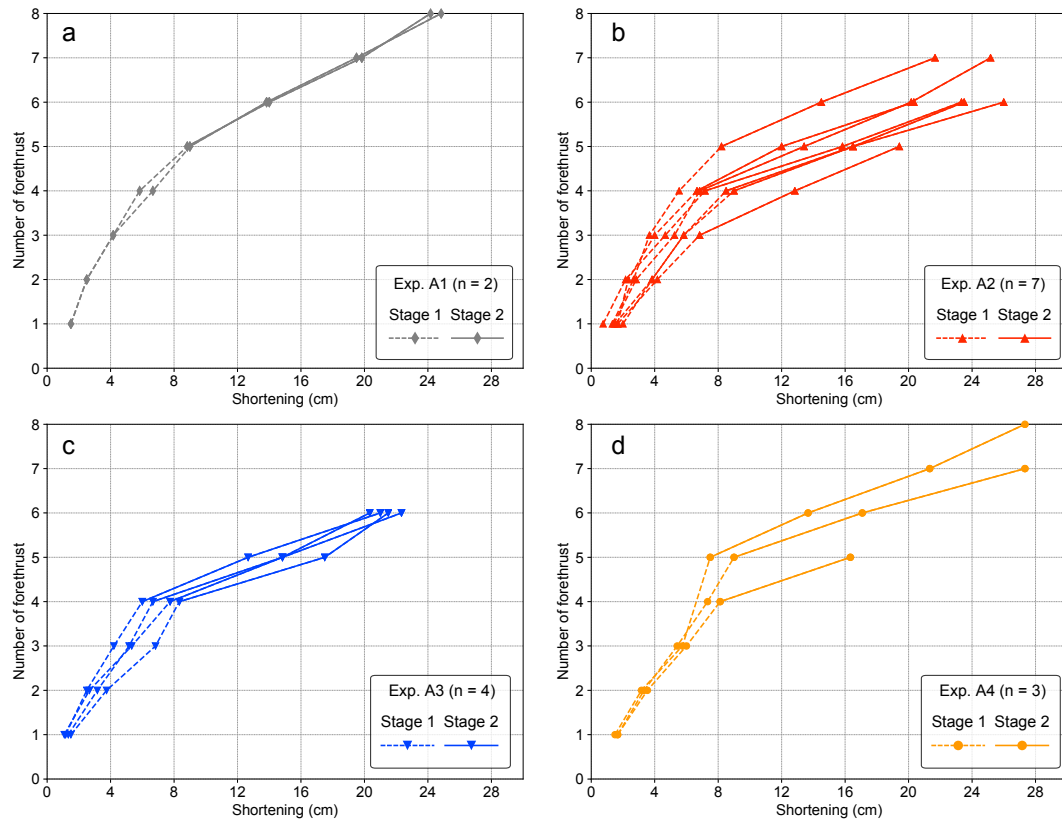


Figure 4. Number of forethrusts with shortening (cm) for all experiments. (a) Experiment without sedimentation (Exp. A1). (b) Experiment with constant sedimentation (Exp. A2). (c) Experiment with fluctuating sedimentation (Exp. A3). (d) Experiment with inversely fluctuating sedimentation (Exp. A4).

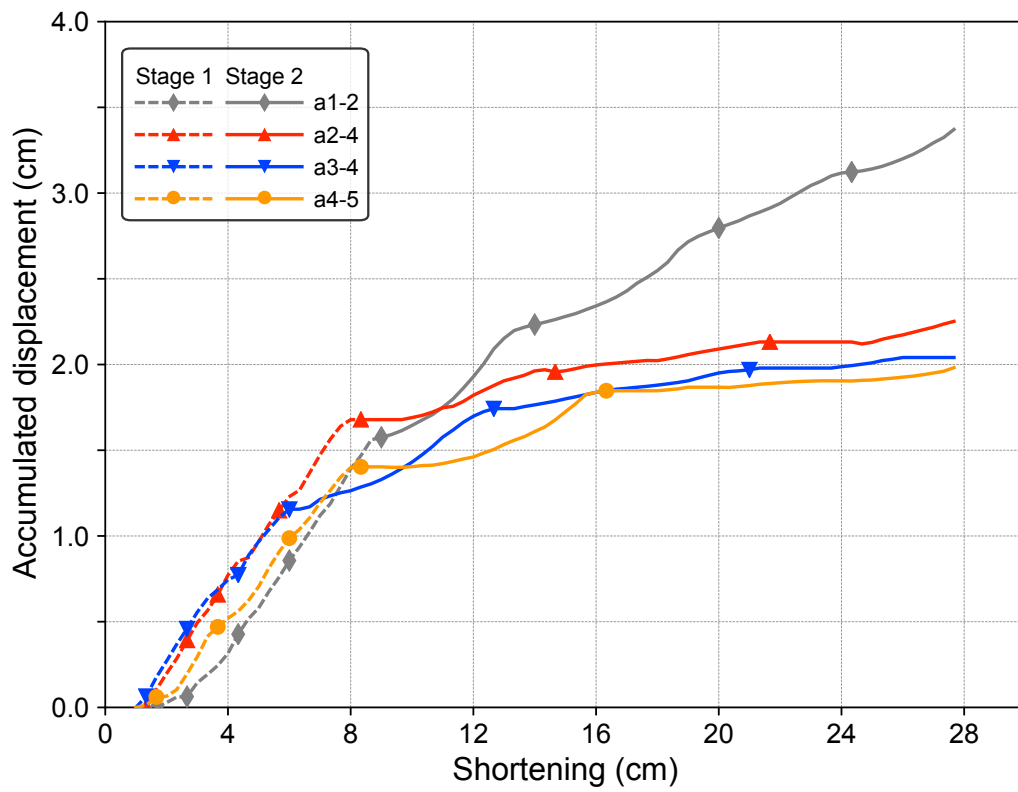


Figure 5. Accumulated displacement on a backthrust of the inner wedge (BT_i).

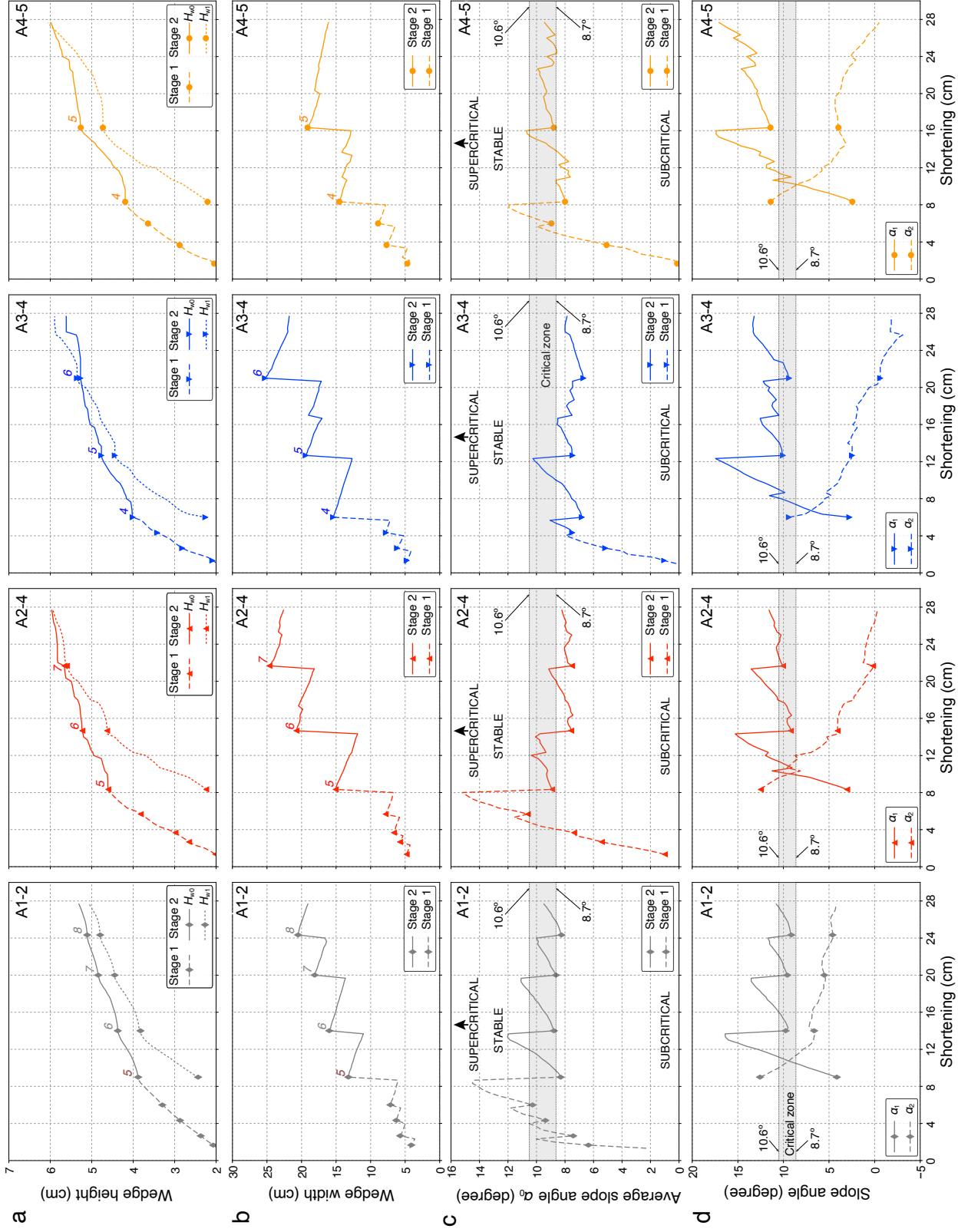


Figure 6. Geometrical parameters of wedges for representative runs. (a) Wedge height, H_{w0} and H_{w1} . (b) Wedge width, L_w . (c) Average taper angle of the entire wedge, α_0 . (d) Slope angles of the outer wedge (α_1) and the inner wedge (α_2). Symbols with numbers indicate the nucleation points of forethrusts. Grayish bands in (c) and (d) indicate critical zones of the taper angle calculated based on critical taper theory (cf. Dahlen, 1984).

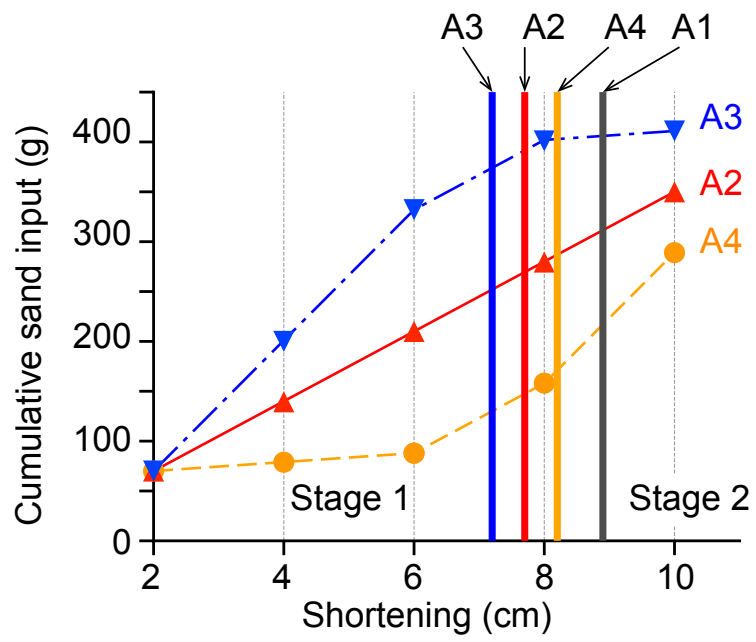


Figure 7. Shortening lengths required to initiate the transition from stage 1 to 2 (horizontal axis). Amounts of cumulative sediment input for Exp. A2–A4 (vertical axis).

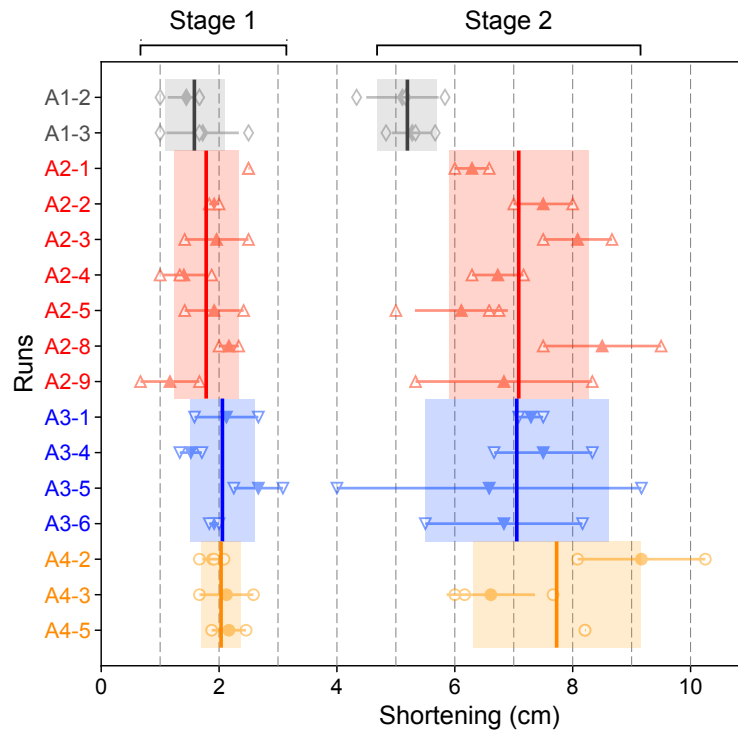


Figure 8. Intervals of forethrust nucleation in stages 1 and 2 for all runs. Open and solid symbols indicate individual and mean intervals for each run, respectively. Solid vertical lines and shaded area indicate the averages and standard deviations of the mean, respectively, of the shortening lengths for forethrust intervals for each case from Exp. A1 to Exp. A4.

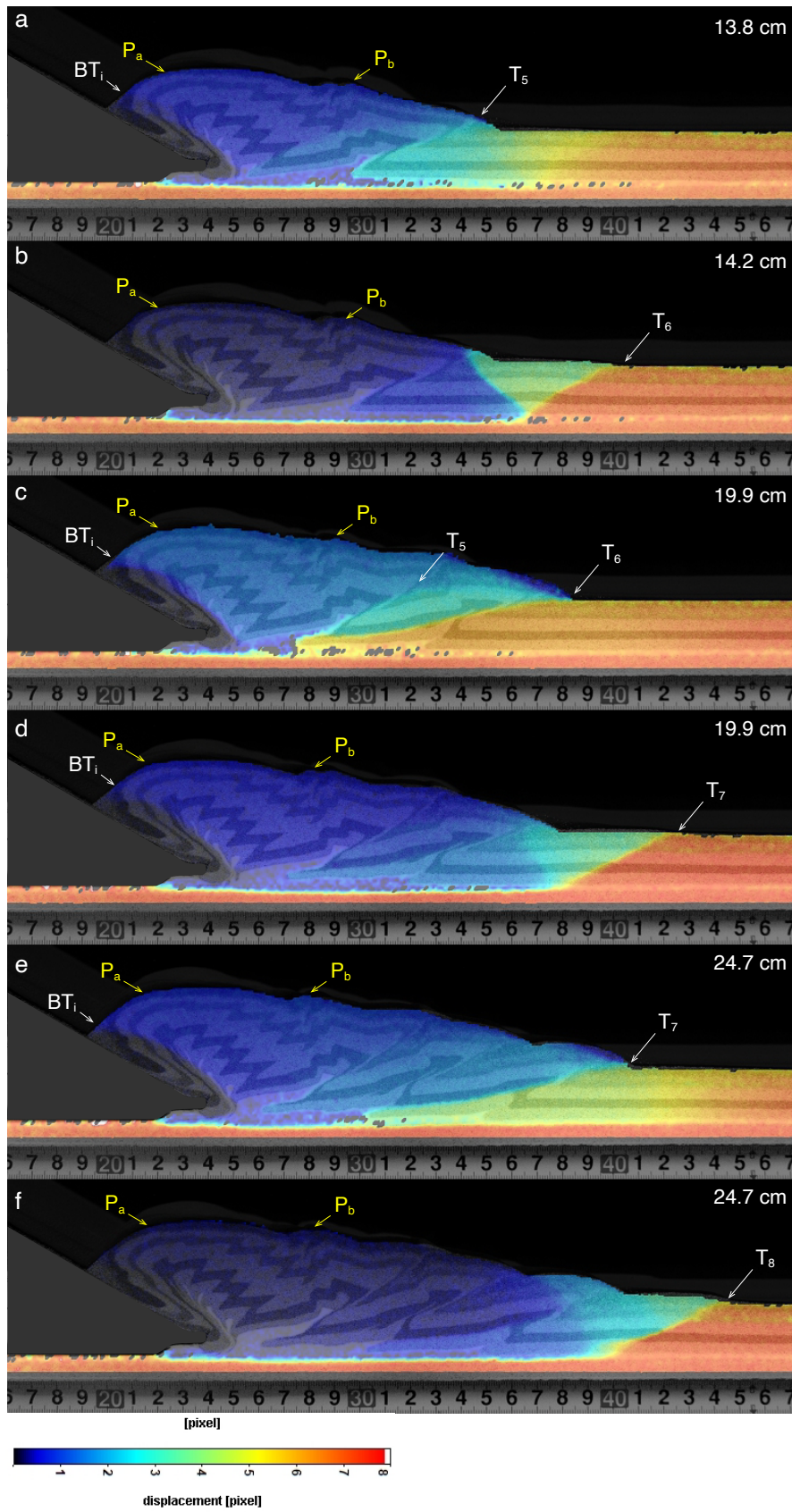


Figure 9. Representative images of incremental displacement (velocity length) obtained from DIC analysis for Exp. A1-2.

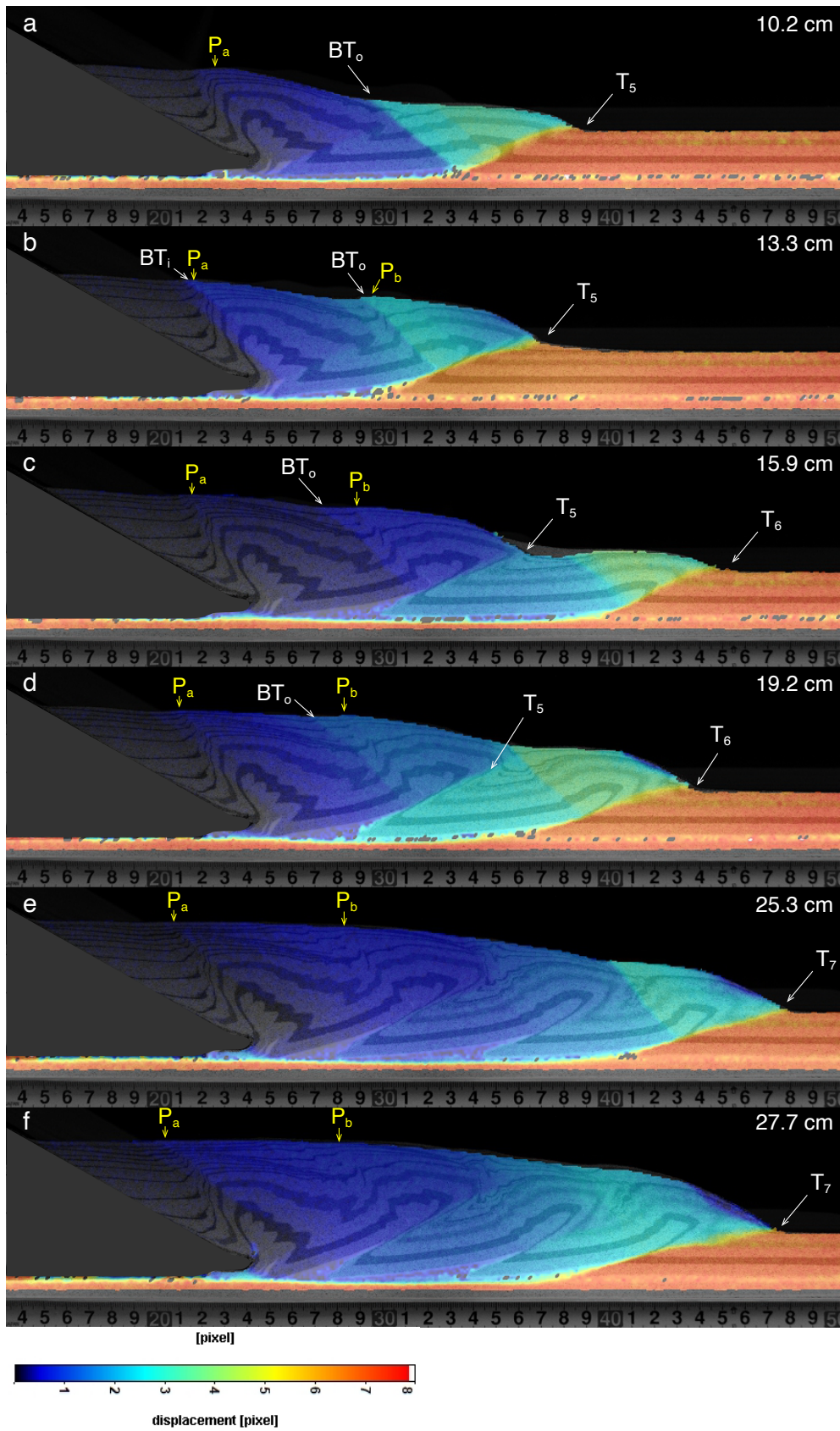


Figure 10. Representative images of incremental displacement (velocity length) obtained from DIC analysis for Exp. A2-4.

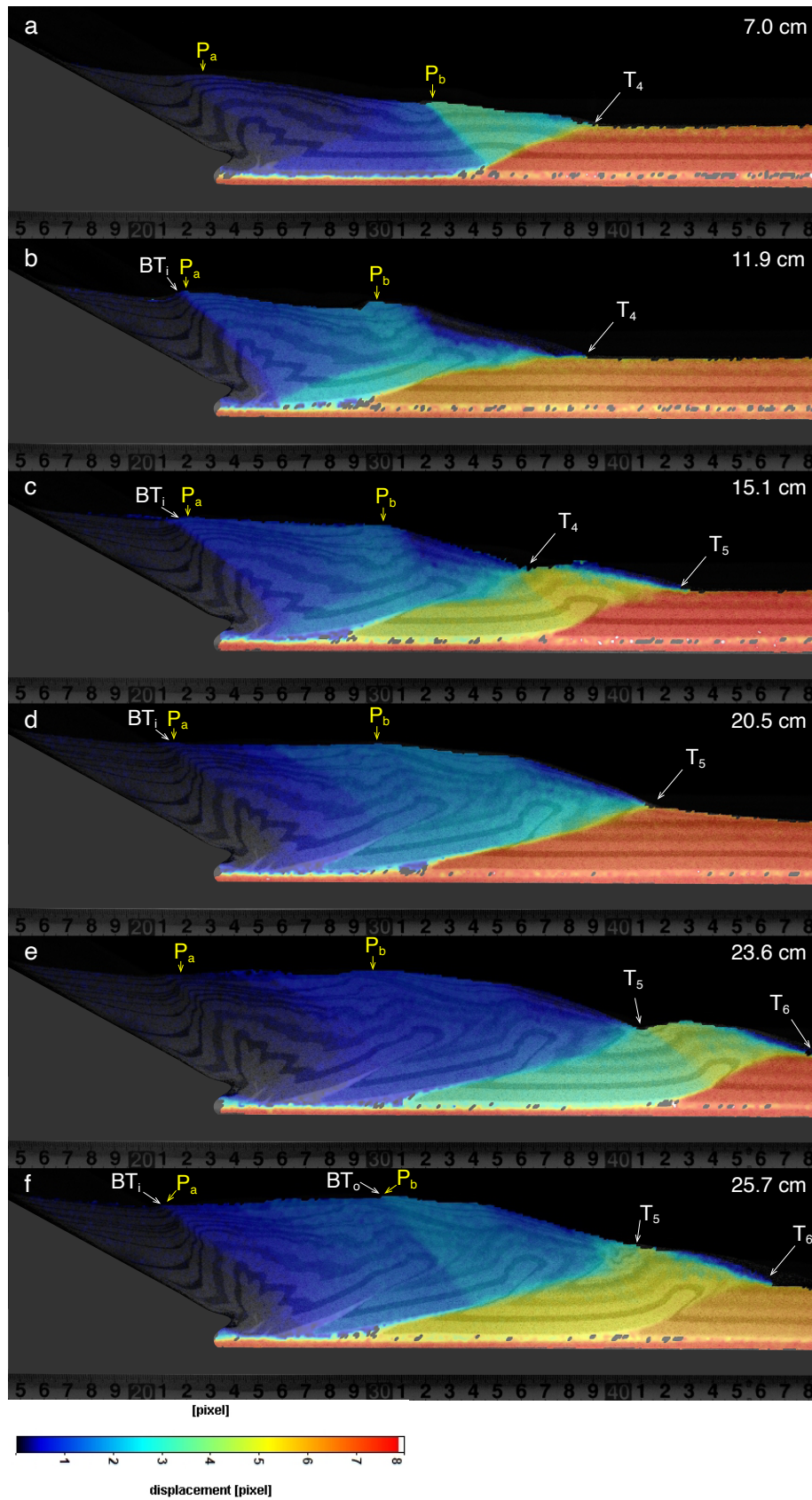


Figure 11. Representative images of incremental displacement (velocity length) obtained from DIC analysis for Exp. A3-4.

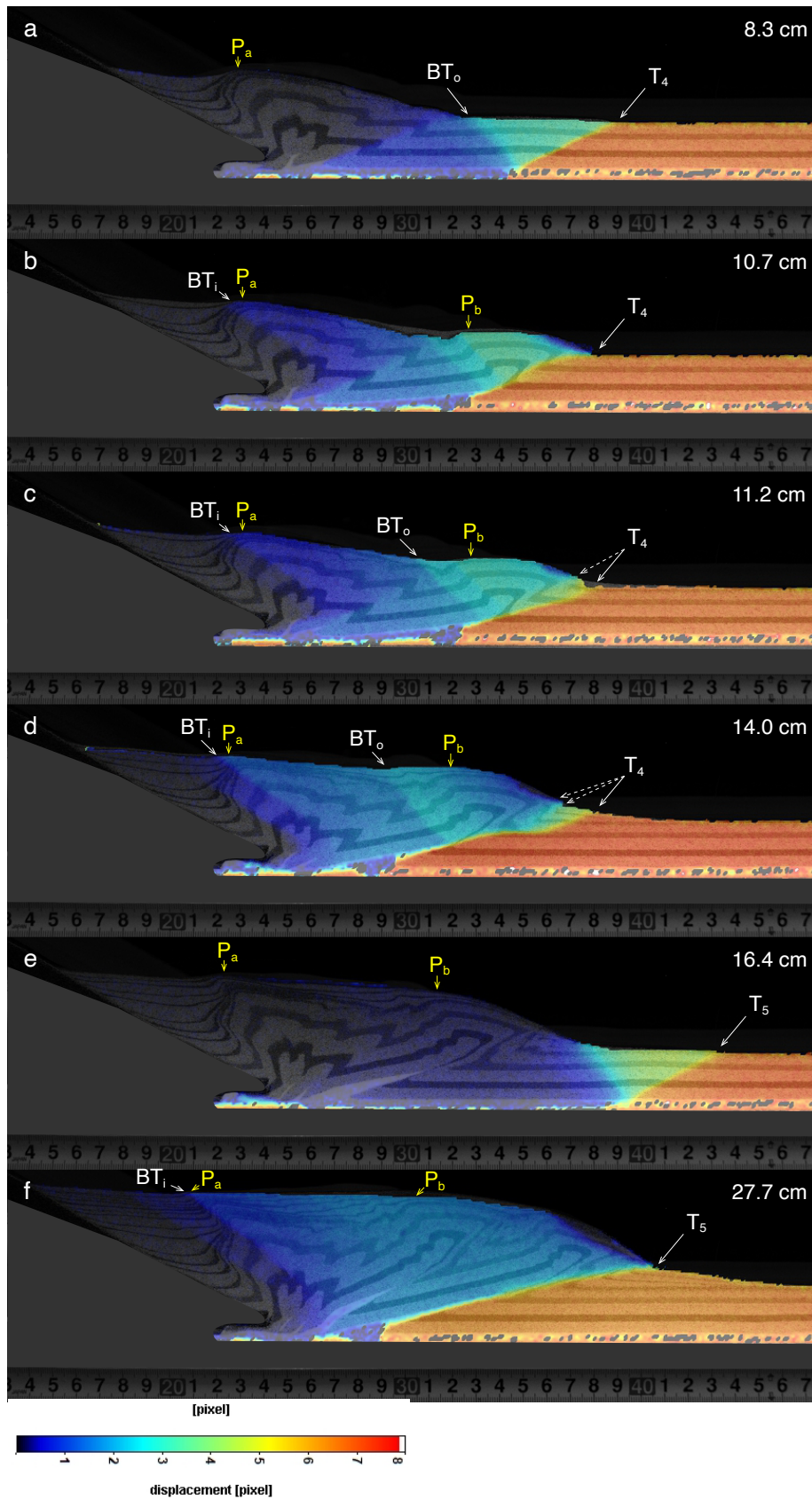


Figure 12. Representative images of incremental displacement (velocity length) obtained from DIC analysis for Exp. A4-5.

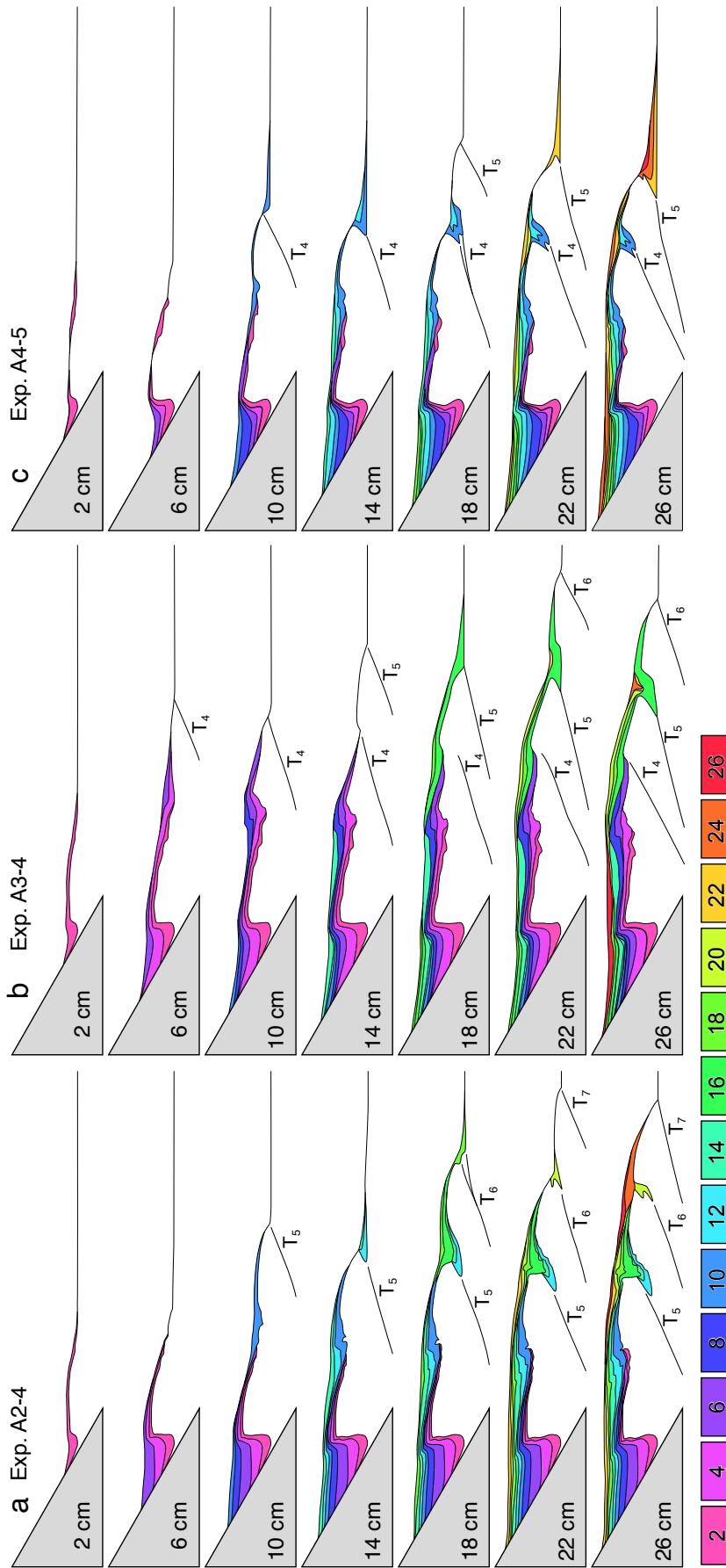


Figure 13. Traces of basin stratigraphy for every 4 cm of shortening.

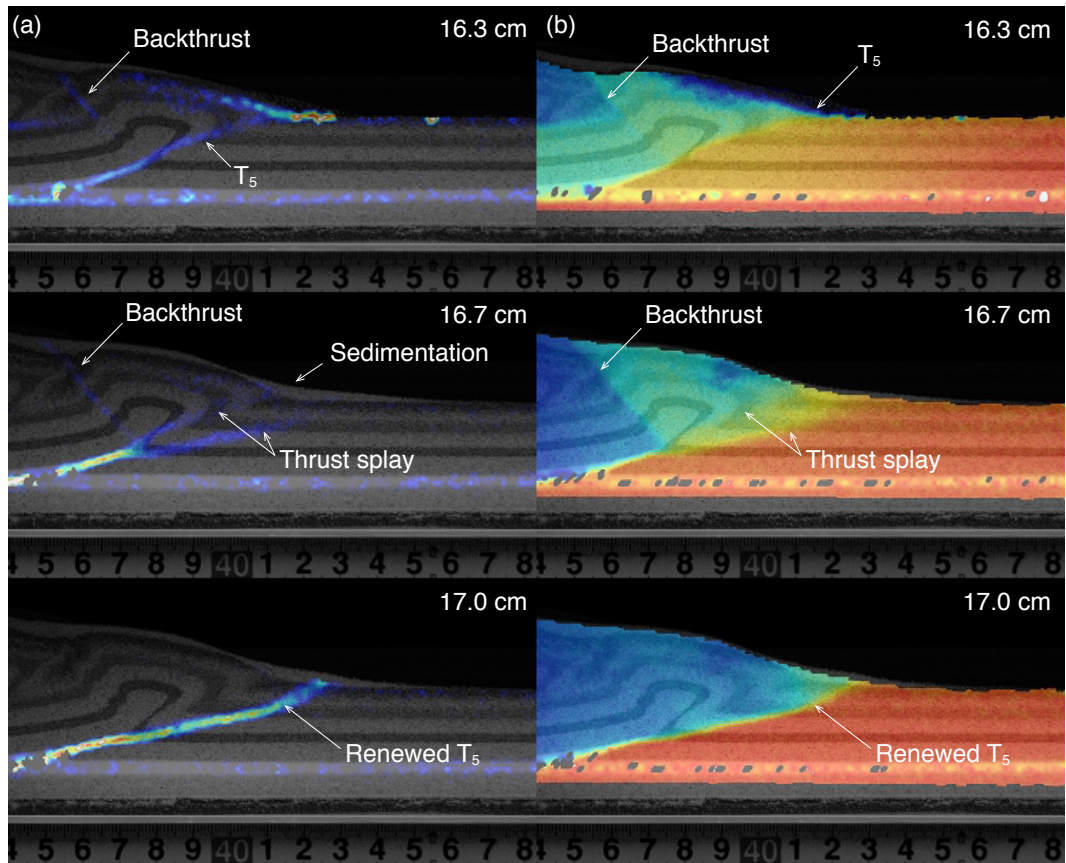


Figure 14. Time-series DIC images showing splay faults from the forethrust tip (Exp. A3-4).

(a) Shear strength. (b) Incremental displacement (velocity length).

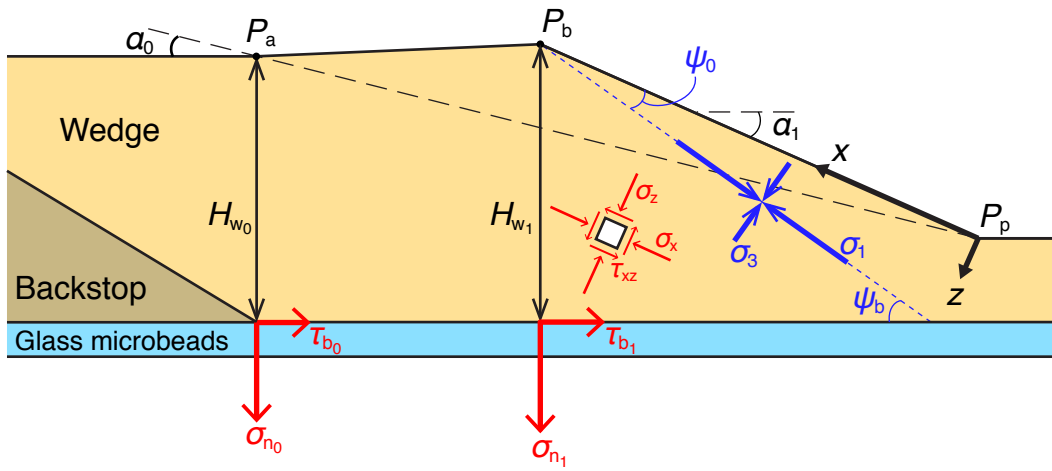


Figure 15. Cross-section of an accretionary wedge with coordinate axes x and z , and angles α_0 , α_1 , ψ_0 , and ψ_b . The angle between the maximum principal stress σ_1 and the coordinate axis x is ψ_0 .

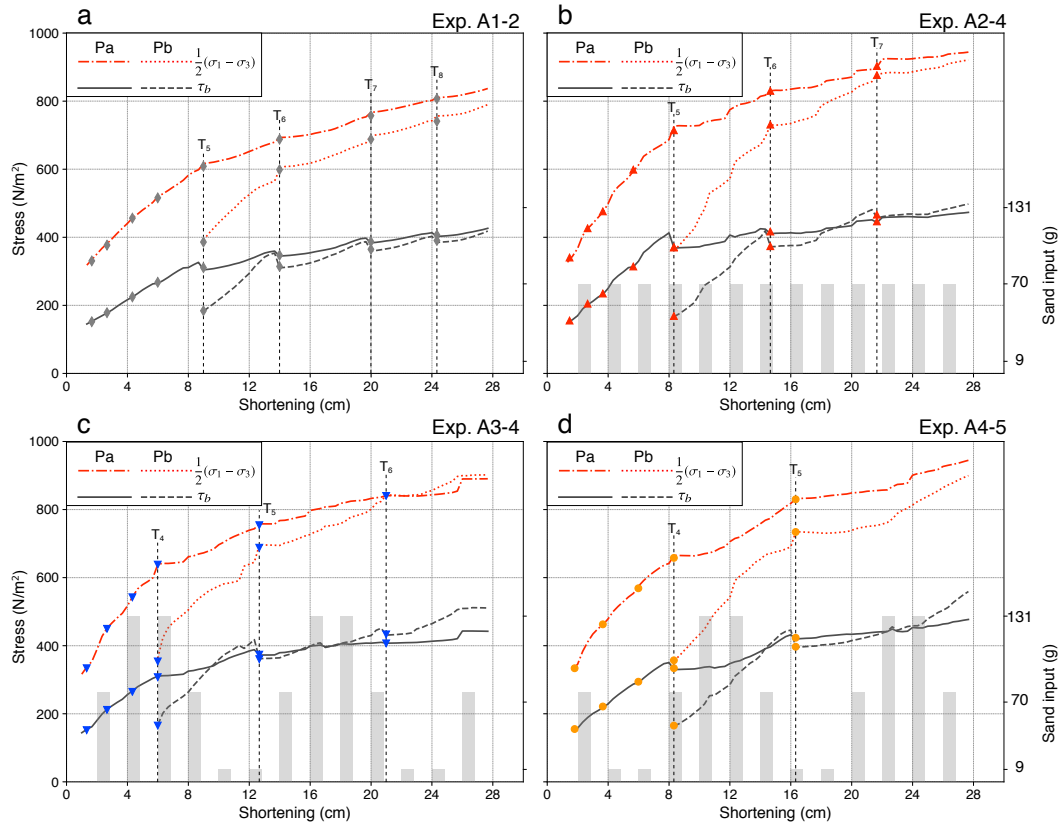


Figure 16. Differential stress $\frac{1}{2}(\sigma_1 - \sigma_3)$ and shear stress τ_b at the bases of P_a and P_b (left vertical axis) and amount of sediment input (right vertical axis).

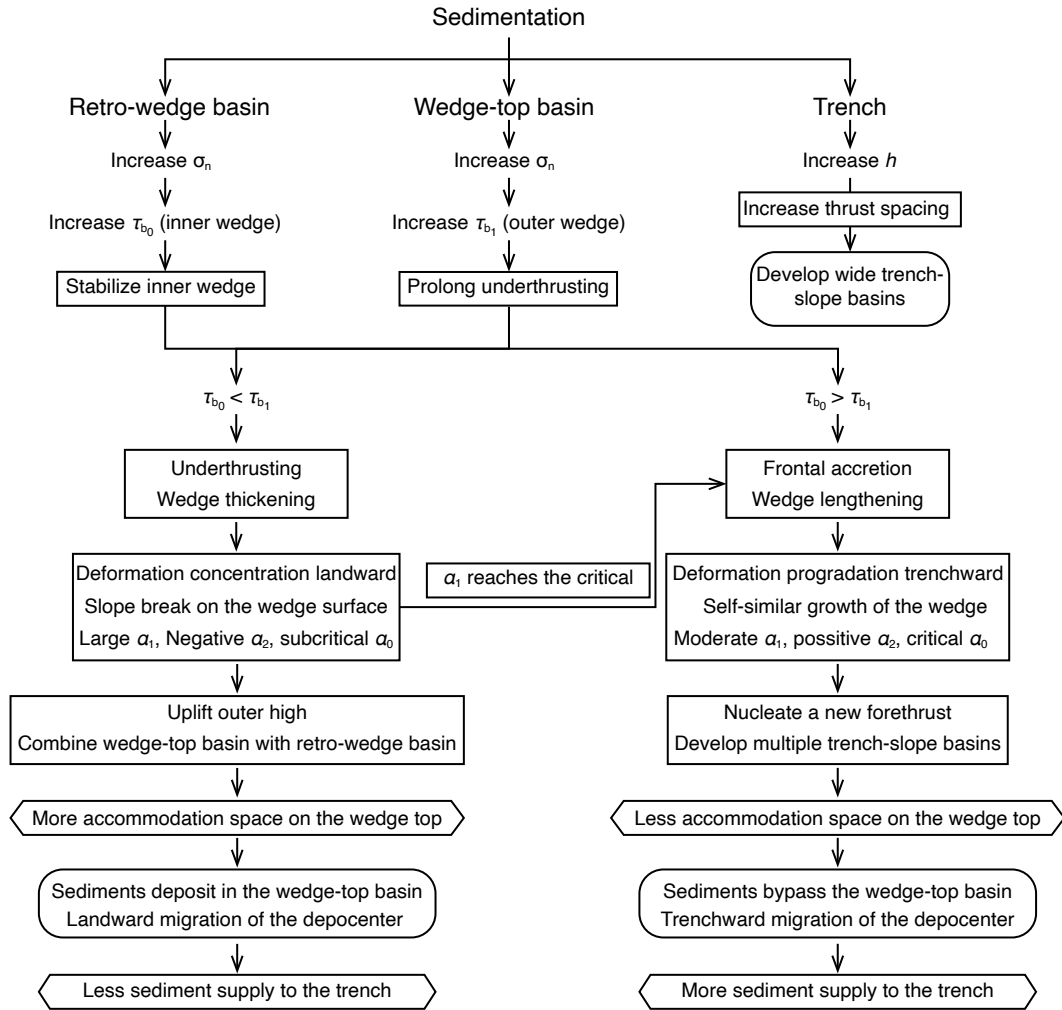


Figure 17. Flow diagram summarizing the interactive relationship between sedimentation (hexagons), wedge deformation (rectangles), and basin evolution (rounded rectangles).

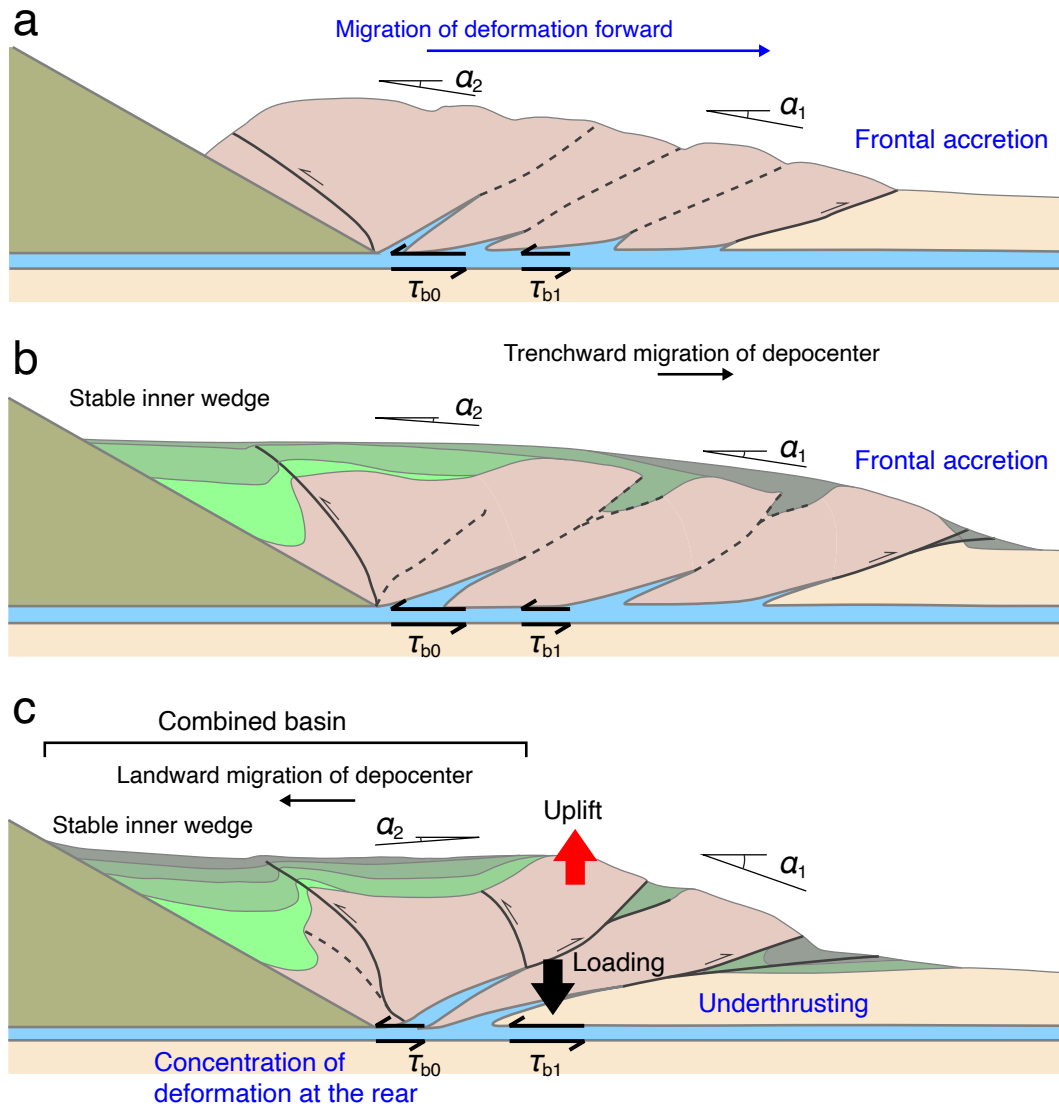


Figure 18. Schematic models of forearc basin formation corresponding to syntectonic sedimentation and accretionary wedge growth. (a) Accretionary wedge without sedimentation. (b) Forward migration of the depocenter in association with progradation of deformation front when the basal resistance on the trenchward side is smaller than on the landward side. (c) Landward migration of the depocenter caused by underthrusting of the incoming layer when the basal coupling at the décollement is stronger than the pre-existing sliding surface.